Ocean Engineering 295 (2024) 116970

Contents lists available at ScienceDirect

Ocean Engineering

journal homepage: www.elsevier.com/locate/oceaneng

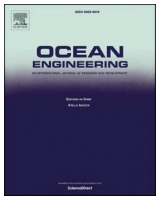

Research paper

The aero-hydrodynamic interference impact on the NREL 5-MW floating wind turbine experiencing surge motion

Ali Alkhabbaz [a,*], Hudhaifa Hamza [b], Ahmed M. Daabo [b], Ho-Seong Yang [c], Min Yoon [d], Aisha Koprulu [e], Young-Ho Lee [c]

[a] Mechanical Engineering Department, College of Engineering, University of Mosul, Mosul, 41002, Iraq
[b] Mining Engineering Department, College of Petroleum and Mining Engineering, University of Mosul, Mosul, 41002, Iraq
[c] Center for Offshore Wind & Green Hydrogen Ammonia Research, Korea Maritime and Ocean University, Busan, 49112, South Korea
[d] Mechanical Engineering Department, Korea Maritime and Ocean University, Busan, 49112, South Korea
[e] Aeronautical Technical Engineering Department, Technical College, Al- Kitab University, Kirkuk, 36001, Iraq

ARTICLE INFO

Keywords:
CFD simulation
Dynamic fluid body interaction
Floating offshore wind turbine
Overset mesh
Semi-submersible platform

ABSTRACT

The present work seeks to explore how the surge response of a semi-submersible platform affects the aerodynamic performance and wake properties of a 5-MW Floating Offshore Wind Turbine (FOWT) when subjected to fully coupled wind-wave load conditions. In order to attain a more comprehensive understanding of the impact of platform surge displacement, a comparative analysis of the aerodynamic performance and wake characteristics was conducted. This analysis involved comparing a floating turbine experiencing surge motion with a conventional floating turbine operating under stable fixed-platform conditions. This simulation employs an overset mesh technique to accurately capture the impact of the semi-submersible platform's surge response on both the aerodynamic behavior and wake properties. Furthermore, the integration of Dynamic Fluid Body Interaction (DFBI) and Volume of Fluid (VOF) approaches is utilized to precisely understand the aero-hydrodynamic interaction and simulate the water-air interface surface. A thorough analysis was conducted to assess aerodynamic performance, catenary analysis, and hydrodynamic reactions by comparing the results obtained from CFD simulations with those acquired from the FAST and OrcaFlex codes. The CFD findings indicate a significant impact of the platform surge response on the apparent wind velocity perpendicular to the rotor plane, which arises from the combined effects of the incoming wind velocity and surge-induced velocity. Moreover, the velocity recovery of the wake flow downstream of the rotor is faster during surge motion than that of the fixed-bottom turbine. The importance of this finding is especially relevant in wind farm scenarios marked by diminished aerodynamic interference between adjacent turbines. Furthermore, CFD investigations and visualizations are carried out on shedding vortices in the wake, tower-blade tip interference, and tension force of the mooring lines. These aspects cannot be adequately captured using potential codes.

1. Introduction

In contemporary times, the increasing need for environmentally friendly energy sources has led to a substantial amount of scholarly investigation concerning blue energy mechanisms capable of effectively harnessing energy derived from tides, waves, wind, and currents (Contestabile et al., 2017; Viviano et al., 2016; Segura et al., 2018; Stewart and Muskulus, 2016a; Vicente et al., 2009; Edirisinghe et al., 2023). Among various sources of renewable energy, wind power possesses great potential, as it is inexhaustible, clean, and aboriginal. As announced in the global wind energy report in 2021, the cumulative onshore and offshore wind turbine installations worldwide exceeded 742 GW in 2020 (Council). Offshore wind energy offers many advantages compared to land-based wind power (Jonkman, 2007). At sea, the space is necessary to install farms of wind turbines and it is more readily available. The wind source is also more abundant and the speed is generally stronger and consistent as it is not affected by buildings, trees, etc. Moreover, relocating wind farms to more remote offshore areas could further reduce visual pollution while offering more suitable fishing conditions (Henderson et al., 2003; Musial and Butterfield, 2004). Hence, the state

* Corresponding author.
E-mail address: ali.alkhabbaz@uomosul.edu.iq (A. Alkhabbaz).

https://doi.org/10.1016/j.oceaneng.2024.116970
Received 29 November 2023; Received in revised form 21 January 2024; Accepted 30 January 2024
Available online 3 February 2024
0029-8018/© 2024 Elsevier Ltd. All rights reserved.

of the art in offshore wind energy potential production and the economic viability of offshore wind energy farms reflect several key trends and considerations, such as potential production, economic viability, and environmental Impact and sustainability (Pantusa et al., 2020; Soukissian et al., 2017; Pantusa and Tomasicchio, 2019; Balog et al., 2016). Globally, offshore wind energy has experienced substantial capacity growth in terms of potential production, attributed to the deployment of larger and more efficient turbines. Moreover, ongoing efforts to decrease the levelized cost of energy (LCOE) for offshore wind involve innovations in installation techniques, project development processes, and supply chain optimization. Furthermore, extensive environmental impact assessments are undertaken to reduce the ecological footprint of offshore wind farms, thereby ensuring sustainable development (Martinez and Iglesias, 2022; Daabo et al., 2020a, 2020b).

Over the years, various types of mounted-bottom foundations for offshore wind turbines have been investigated such as monopile substructures (Zhou et al., 2019; Jung et al., 2015; Frick and Achmus, 2020), and jacket substructures (Häfele et al., 2018, 2019; Shi et al., 2015). These offshore turbines are mostly installed in shallow waters by driving monopiles or fixing concrete gravity bases into the seafloor. Thus, even though these types of wind turbines are considered mature, they are not economically viable in deep seas. Moreover, the offshore potential resource in most countries worldwide is available in deep waters. In addition, the capacity factor is usually greater offshore than onshore or in shallow waters due to the abundance of stronger wind speeds throughout the year. In this regard, the technology of harvesting wind power in deep seas has experienced rapid growth in the last decade. One possible method is to place wind turbines on floating foundations fixed at the seabed. Depending on the mooring systems, water depth, and ballast approaches, various floating configurations are proposed for offshore wind turbines. These floaters are initially employed for offshore gas and oil production. Considering the method of stability achievement and the water depth in which the turbine is installed, the floating platforms can be classified into three major categories as follows: (a) Spar buoy platform, this structure relies on heavy deep ballast to provide resistance to overturning moments. The spar is typically a long, hollow cylinder with a large mass existing at the deepest part of the buoy. The mass within the ballast can be adjusted. Thereby, the spar can flow higher or shallower within the water column as these forms a part of the stability requirements (Rodriguez and Jaworski, 2020; Leimeister et al., 2020; Lerch et al., 2019; Arany and Bhattacharya, 2018; Tomasicchio et al., 2018). (b) Tension leg platform is a large vertical floating module that is constantly moored using tendons or tethers placed at the corners of each structure. These tethers, which are referred to as tension legs, are designed with relatively high axial stiffness, resulting in the elimination of substantially all vertical motion of the platform (Tian et al., 2021; Wu et al., 2021; Zhang et al., 2020; Chow et al., 2019). (c) Semi-submersible platform: a floating structure that relies on horizontally spaced pontoons which can be connected via a lot of bracings or beams. The pontoon has a positive buoyancy to contract both the weight of the mooring system and wind turbine as well as provide rotational stability of the platform to overcome roll and pitch motions within the tower and RNA. Heave motions are typically created by heave plates that are connected to the bottom of the pontoon which add drag resistance to up and down motions within the water (Kim and Shin, 2020; Chen et al., 2020; Bagherian et al., 2021).

Although placing offshore wind turbines on an adapted floating structure integrated with a mooring lines system reduces the cost of deep-sea installation, it simultaneously increases the technological challenges. One of the most common challenges is that offshore structures may be exposed to highly nonlinear hydrodynamic loads due to extreme environmental conditions like gust bumps, extremely excited waves, intense currents and strong wind. Further, offshore structures and slender cylindrical bodies might be exposed to some physical phenomena, such as vortex-induced motions, and wave run-up (Shan et al., 2011; Aristodemo et al., 2011). The connection between the rotor of the offshore turbine and its floating basic is established through a lengthy tower, thereby affecting the platform motion and hydrodynamic response by the aerodynamic loads about torque and thrust. Concurrently, the movement of the platform also influences the orientation and position of the offshore turbine rotor. with the six-DOF. Additionally, the analysis of Floating Offshore Wind Turbines (FOWTs) becomes increasingly intricate to combined effects of dynamic excitation caused by the mooring system, ballast options and wind-wave loads. However, very little testing has been done on full-scale FOWTs and a majority of the data required for analysis remains confidential, thereby rendering it inaccessible to researchers (Stewart and Muskulus, 2016b). Moreover, full-scale prototype testing is much more expensive and is not economically feasible. Therefore, several experimental tests were implemented on different scaled-down FOWTs models in wave tanks using various concepts. A 1/48th scale tension-leg platform was tested by Ward et al. (2021), adopting a conceptual hanging-mass FOWT design. Goupee et al. (2014) examined three different scaled-down floating wind turbines under various loads of wind-wave. The distinctive benefits and drawbacks of each levitating platform were documented. Another work of 1/50th scale OC3 spar concept FOWT is experimentally tested by Duan et al. (2016). The wake properties of a semi-submersible FOWT are analyzed by Xiong et al. (2020) using a wave flume and wind tunnel. It is concluded that the center of the raised Reynolds stress distribution drifts upward. In contrast, the center of mean velocity deficit distribution stays at a constant height. Some studies have also been conducted considering the influence of nonlinear diffraction wave loads (Li and Bachynski, 2021), the aerodynamic forces on the top-tower of 1/22.5th scale model of spar-buoy FOWT (Utsunomiya et al., 2009), the actuator disk concept to replicate aerodynamic thrust on 1/105th scale FOWT rotor (Roddier et al., 2010), the effect of hydrodynamic coefficients on 1/100th and 1/40th scale tension-leg platforms (Myhr and Maus, 2011; Myhr and Nygaard, 2014, 2015) and the finding obtained were compared with OC3-HYWIND floating platform.

Based on the aforementioned, scaling laws are essential to scale the empirical data from the model tests to precisely estimate the dynamic properties of a full-scale prototype. However, these scaling laws have some limitations and weaknesses. For instance, Froude-based scaling (Martin, 2009) which is usually adopted for model testing of offshore structures, has some level of inconsistency in the scaling of Reynold number (Intertek et al., 2012). In addition, the experimental test of scaled floating structures is pricey and it is usually not economically feasible. These issues need to be treated through conceptual analysis and design of FOWTs. To better comprehend the dynamics of full-scale FOWTs, a variety of design specifications and numerical modeling tools have been modified. These codes involve various modules in a fully integrated simulation platform such as the aerodynamic forces model (aero), hydrodynamic loads model (hydro) control system (servo), and structural dynamic analysis (elastic). The most well-known numerical tools used for FOWTs analysis are; FAST code, MSC. ADAMS, OrcaFlex, and PanMARE solver (Jonkman, 2009; Wiegard et al., 2021; Orcina, 2012). In the present investigation, both FAST and OrcaFlex analysis tools are employed for a full-scale FOWTs simulation. FAST is a comprehensive numerical tool that involves aerodynamic forces, blade deflection, tower motion, hydrodynamic loads, and mooring system analysis using a quasi-static approach. OrcaFlex is a time domain program that combines aerodynamic forces, hydrodynamic loads, and cable dynamics (Masciola et al., 2013). Both FAST and OrcaFlex are capable of investigating and analyzing the dynamic motions of different design concepts for various floating platforms. However, most of these codes are depend on empirical equations and some correction factors such as; conventional Blade element Momentum theory (BEM), to estimate the aerodynamic loads (Hansen et al., 2006; Hansen, 2000). Furthermore, these models ignore the intricate interaction between the rotor of the wind turbine and its wake. Since floating turbines move in and out of its own wake, Sebastian and Lackner (2013) reported that BEM remains not

sufficient for estimating the aerodynamic behavior of FOWTs. The influences induced by blade tip vortices and the fluid viscosity could not be efficiently captured using the BEM approach (Alkhabbaz et al., 2021). In addition, the hydrodynamic module used in these numerical tools is established on the theory of the potential flow, where the effect of viscous flow is not considered (Jonkman, 2009; Masciola et al., 2013). Thereby, additional damping coefficients obtained from experimental data or determined using some empirical models such as the Morison equation are needed. In this regard, external codes such as WAMIT (Lee et al., 1991) and OrcaWave (Orcina, 2012) are essential to provide the required hydrodynamic coefficients, added mass matrix, hydrostatic forces, added damping, as well as the platform induced (radiation) and wave-induced (diffraction) loads. Although, these external codes are well coupled with FAST and OrcaFlex numerical tools, some physical phenomena are still not fully captured such as, wave run-up, breaking waves, vortex-induced vibration by currents, potential loading from sea ice and floating debris, as well as the flow separation on the floating platform due to the viscous flow (Shan et al., 2011; Diaconu, 2013; Butterfield et al., 2007; Carlson and Modarres-Sadeghi, 2018). In contrast, The Computational Fluid Dynamics (CFD) technique can directly evaluate the hydrodynamic forces acting on a buoyant structure, in both the lateral and longitudinal orientations. The impact of flow separation caused by viscous flow is also taken into account. Further, CFD technique can examine the intricate flow interaction between the turbine rotor and its own wake on one side, and between the rotor and the floating platform on the other side. Accordingly, it is necessary to make a comparison between CFD outcomes of FOWT and those acquired using different numerical tools.

Numerous investigations have been carried out employing computational fluid dynamics (CFD) simulation to examine the hydrodynamic load and dynamic response of various categories of floating platforms, including the Spar-buoy concept (Beyer et al., 2013), and the semi-submersible platform (Tran and Kim, 2015a; Benitz et al., 2014, 2015; Zhao and Wan, 2015; Yang et al., 2022). Some CFD investigations were performed to examine the intricate flow interactions between the rotor of wind turbine and the floating platform caused by the coupled wind-wave loads. The DFBI approach was employed by Tran and Kim (2016a) to investigate the influence of six degrees of semi-submersible platform motions on a full-scale FOWT aerodynamic performance using an overset mesh technique. A methodical comparison between CFD outcomes with those gained from the NREL-FAST code showed a good correlation with some slight discrepancies in the aerodynamic thrust and the average tension of the mooring cable. More examinations have been implemented to simulate the influence of various platforms on the dynamic behavior of a full-scale FOWT, such as tension-leg platform (Nematbakhsh et al., 2015), OC3 HYWIND-spar buoy floater (Li et al., 2015), and OC4 semi-submersible platform (Chuang et al., 2020). Liu et al. (2016) demonstrated a CFD investigation for NREL phase VI wind turbine with only three superimposed degrees of platform movements like Surge, Pitch, and Heave. Results reveal a strong effect of the specified platform motion on the behavior of the aerodynamic in terms of thrust and power. Another work for a 5-MW FOWT is performed by Liu (Liu et al., 2017) with only three degrees (Surge, Pitch, and Heave) of freedom of platform motions being considered. It is reported that the floating platform was slightly displaced in the surge orientation due to the influence of aerodynamic thrust. Tran and Kim (Toan Tran et al., 2015; Tran and Kim, 2016b) investigated a full-configuration FOWT under various amplitudes and frequencies of a prescribed sinusoidal platform surge motion. They stated that the wave properties (amplitude and frequency) considerably influenced the aerodynamic performance with regard to power and thrust output. The impact of spar buoy platform movement on the hydrodynamic performance of a FOWT is studied by Tran and Kim (2015b) using a high-fidelity CFD simulation. Two degrees of platform motions (pitch and yaw) were only considered in this analysis. The investigation findings depict the presence of a complex interface between the blade tip-induced vortices and the turbine rotor-induced wake.

The foregoing indicates that conducting a CFD simulation of full-scale floating wind turbines poses a challenge for many researchers. This is due to the significant amount of time required, in addition to the need for high-performance computers. Moreover, the six DOFs motion of the floating platform presents an extra difficulty, influencing the aerodynamic performance of the turbine directly. The surge displacement of the platform is a critical degree of freedom (DOF). It is essential to comprehend the responses in surge motion before delving into more complex six DOFs coupled analysis. Additionally, a single surge DOF can be more easily understood and replicated by other researchers. Hence, the current work aims to conduct a high-fidelity CFD simulation of a full-scale wind turbine positioned on the OC4 semi-submersible platform experiencing surge motion. To gain a deeper understanding of the influence of platform surge response on aerodynamic performance and wake flow, the obtained results were compared with the corresponding data of the 5-MW wind turbine when all degrees of freedom were kept fixed. This simulation utilizes an overset mesh technique to accurately capture the influence of the semi-submersible platform's surge response on both the aerodynamic behavior and wake properties of the 5-MW Floating Offshore Wind Turbine (FOWT). Additionally, the incorporation of DFBI and VOF approaches is employed to precisely comprehend the aero-hydrodynamic interaction and simulate the water-air interface surface. The Computational Fluid Dynamics (CFD) investigation was conducted at a rated wind speed of 11.4 m/s and an extreme regular wave height of 7.58m. A systematic comparison of hydrodynamic response, aerodynamic performance, and catenary analysis outcomes was carried out between CFD simulations and those obtained by FAST and OrcaFlex based on Blade Element Momentum (BEM) models.

2. Model description

In this study, the OC4-DeepCWind semi-submersible floating offshore wind turbine is used for modeling and conducting analysis. The floating system comprises the well-known NREL reference wind turbine with rated capacity up to 5-MW at rated wind velocity and rotor speed of 11.4 m/s and 12.1 rpm respectively. It is a utility-scale conventional three-bladed turbine with a rotor diameter of 126 m and a hub height of 90 m. The technical report of NREL outlines the comprehensive specifications for the design in detail (Jonkman et al., 2009). The turbine is placed on a cylindrical tower of 87.6 m in length with top and base diameters of 3.87 m and 6 m, respectively. The floating foundation is based on the Offshore Code Comparison Collaboration (OC4) DeepCWind project. The structure comprises a central pillar measuring 6.5 m in diameter that is coincident with the tower base. Three offset columns with a heave plate attached to each bottom are braced to the central main column through several cross members and pontoons (Robertson et al., 2014). The pontoons have positive buoyancy to contract the weight of both wind turbine and mooring system and to provide rotational stability of the platform to overcome pitch and roll motions. Fig. 1.a displays the CAD model of the considered system.

Several experimental tests on a small scale (1/50th) semi-submersible floating system were performed at Maritime Research Institute Netherland (MARIN's). However, the gross characteristics of the baseline rotor, nacelle, and tower were slightly modified during the manufacturing process. Details about the 1/50th scale test model and setup information could be found in the previous work presented by Coulling (Coulling et al., 2013). In this regard, the gross characteristics utilized in the previous study were adapted in this work to precisely evaluate the CFD outcomes with those of the test model. The total platform mass including ballast water is 13,444,000 kg, where the centre of mass exists 14.4 m under the Still Water Level (SWL). Details of platform gross properties applied in this research are reported in Table 1.

Three fairleads are strategically located at the summit of the heave plate, wherein they are expertly linked to their corresponding anchors,

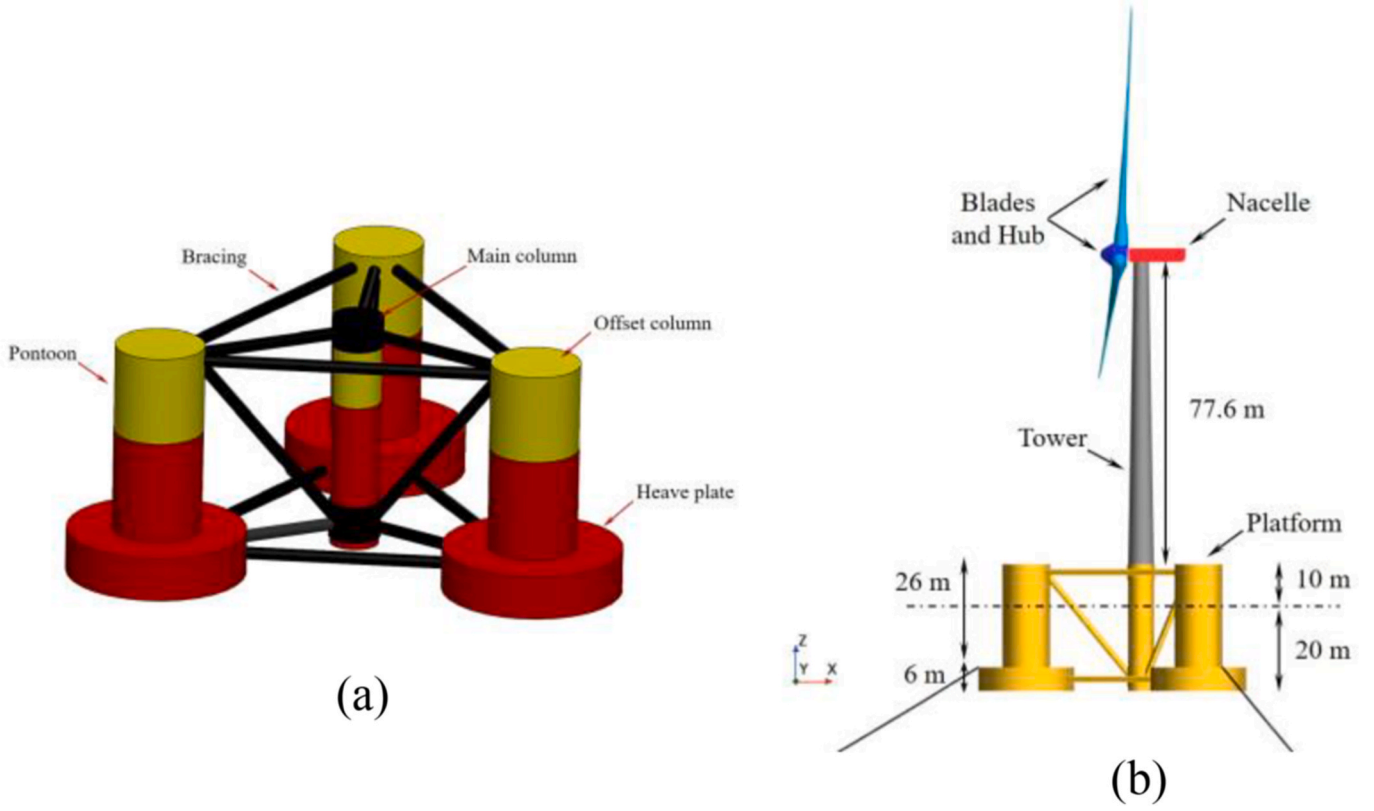

Fig. 1. CAD model of NREL baseline 5-MW FOWT: (a) OC4 semi-submersible platform, (b) Full configuration.

Table 1
Characteristics of full-scale DeepCwind semi-submersible platform (Jonkman, 2007).

Elevation to platform top from MSL	10	M
Total draft	20	M
Center of mass (CM) below MSL	−14.4	M
Platform mass	13,444,000	Kg
Displacement	13,986.8	m^3
Platform roll inertia about CM	8.011 x 10^9	kg m^2
Platform pitch inertia about CM	8.011 x 10^9	kg m^2
Platform Yaw inertia about platform centerline	1.391 x 10^{10}	kg m^2

situated at a profound water depth of 200 m, through the utilization of three catenary mooring lines. The current study employs a wave heading angle of 0° that is aligned with the direction of catenary line-1. This angle corresponds to the angle between two neighboring mooring lines of 120°. Details of mooring system properties are reported in NREL technical report (Robertson et al., 2014). Fig. 1.b demonstrates the full geometry of NREL 5-MW FOWT.

3. Numerical consideration

3.1. High-fidelity CFD simulation

CFD is a useful numerical tool that spans a wide range of application areas such as hydrodynamics of floating bodies, power plants, and aerodynamics of vehicles and aircraft (Karimirad et al., 2018; Versteeg and Malalasekera, 2007). Various elements make up the basic structure of CFD codes such as the definition of the model configuration, boundary and operating conditions, the definition of fluid characteristics, and the mesh generation. This section will briefly discuss all CFD techniques applied in the present simulation.

3.1.1. Boundary conditions

In this work, the adapted flow region associated with the boundary conditions is illustrated in Fig. 2. At the upstream boundary and seafloor, the velocity inlet is applied. Both the exit and the upper surface are provided with a pressure outlet. A non-slip wall condition was imposed for all surfaces of the wind turbine body structure. Moreover, all structural components including blades, hub, nacelle, tower, and the platform responded as a rigid body motion. Furthermore, the sidewalls of the entire flow domain were defined as symmetric boundaries.

The aerodynamic performance of a wind turbine is strongly influenced by the intense spiral vortices in its wake (Alkhabbaz et al., 2022), thus, the flow region must be long enough to avert unwanted aerodynamic interactions. In this regard, the entire flow region is extended up to 1200 m in the (x) direction and 500 m in both (y) and (z) directions. The wind turbine was initially placed at a site of 300 m from the upstream boundary.

The mooring system is employed to restrict the movement of a floating system, to provide a high stability level, and sufficiently minimize the impact of circumferential loads like wind, current waves and tide. Several types of mooring systems exist, either catenary lines, which are used for semi-submersible and spar buoy platforms, or taut-leg mooring system, which is utilized for tension-leg platform concepts (Castro-Santos and Diaz-Casaa, 2016). The catenary coupling element approach was adopted to model three elastic mooring cables between the platform and the seabed. The mooring line restoring forces are solved using a quasi-stationary representation. This implies that the catenary always has a simple form. This strategy is quite appropriate for body motions, which are sufficiently slow compared to the wave velocity in the catenary (User manual).

3.1.2. Wave free surface

In CFD simulation, the free surface wave is represented as a connection between two-phase of flow. Several multiphase models are proposed to simulate the fluid-induced dynamic motion and to evaluate

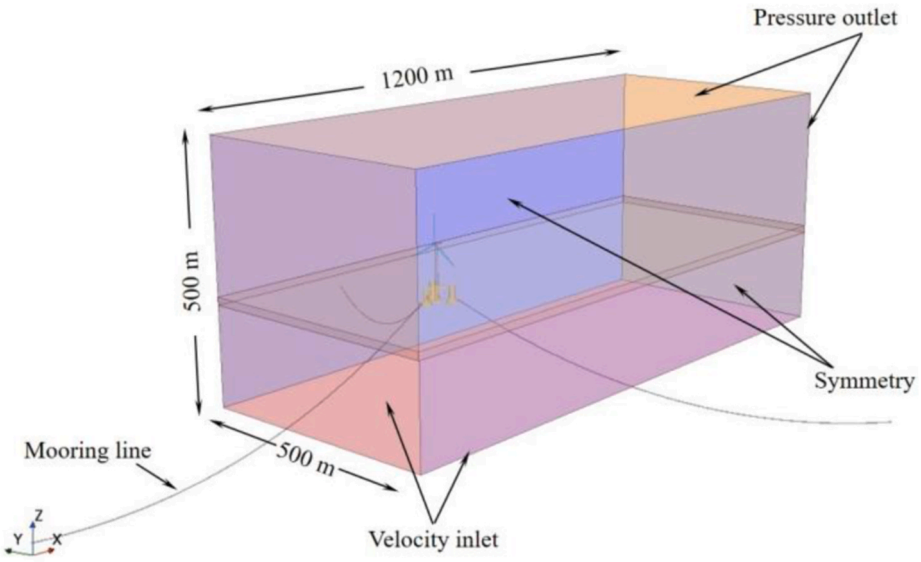

Fig. 2. The flow region with associated boundary conditions.

the hydrodynamic loads on floating structures. In the present study, the VOF approach (Hirt and Nichols, 1981) relay on the Eulerian method was adapted to represent the wave-free surface and to capture the light fluid (air)-heavy fluid (water) interface. This model considers that physical properties such as velocity, temperature, and pressure are common to all phases of flow. Thereby, the governing equations of mass conservation and momentum conservation could be applied in the two-phase flow. The VOF model basically depends on allocating a specific function to each mesh cell in the computational region. For instance, setting the function value equal to one to represent the heavy fluid (water), whereas, the light fluid (air) can be represented if the value equals zero. Moreover, the filled volume ratio is considered when assigning the function value to mesh cells that are partially filled. Fig. 3 illustrates the volume fraction adopted in the present investigation.

Furthermore, to ensure that no wave reflection will occur on far-field boundaries, a damping function was set up over a distance of 300 m from the outlet boundary surface. This function is a combination of linear and quadratic damping coefficients, which are added to the momentum equations as source terms to eliminate the effect of the vertical velocity component of the flow over a certain distance. The new term c_s added by the sponge layer is expressed as (Larsen and Dancy, 1983):

$$c_s = -\rho\mu_s \boldsymbol{V} \tag{1}$$

$$\mu_s = \begin{Bmatrix} \delta\left(\dfrac{x - x_o}{L_s}\right), if\ x > x_o \\ 0, if\ x \le x_o \end{Bmatrix} \tag{2}$$

Where, μ_s refers to the artificial viscosity. The δ is the damping strength of the sponge layer, and x represents the coordinate of the grid cells in x-direction. Both x_o and L_s denote the start position and the length of the sponge layer, respectively. Fig. 4 illustrates an overview of the regular wave theory and the effect of the sponge layer.

3.1.3. Numerical scheme

A finite volume approach was applied to discretize the governing equations, which are solved numerically using the segregated flow model. The Semi-Implicit Method for Pressure Linked Equations (SIMPLE) (Patanker, 1980) was employed to actualize the pressure-velocity coupling. It is a quite popular algorithm in suits used in a lot of CFD codes. The two key tricks of the SIMPLE algorithm are to derive an equation for pressure from the momentum and continuity equations and then it can be used to calculate the pressure field. Second, to derive a

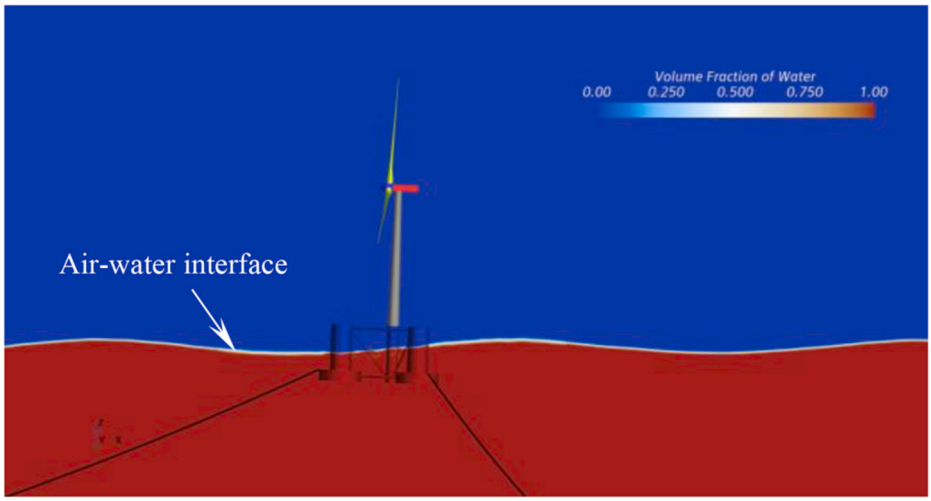

Fig. 3. Modeling of wave free surface.

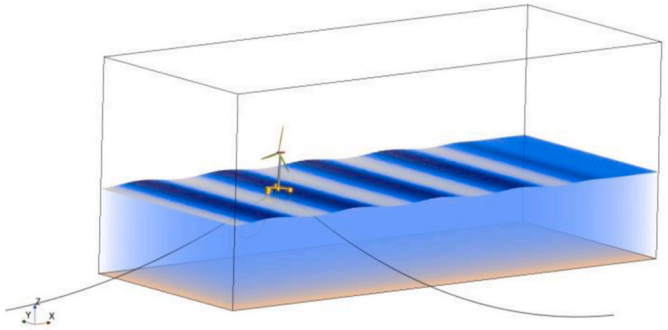

Fig. 4. Overlooking of the wave free surface and the effect of sponge layer.

corrector for the velocity field, so that it satisfies the continuity equations. Besides, a second-order central difference and second-order upwind schemes were applied to accurately solve the time discretization of transient flow and convection terms, respectively. Furthermore, Dynamic Fluid Body Interaction (DFBI)module was employed to simulate the motion of a rigid body in response to the fluid forces, moments, gravitational forces, as well as the forces exerted by the mooring lines on a 6-DOF body. It basically relies on solving the governing equations of motion by calculating the resultant force and moment acting on a rigid body, which eventually leads to finding the new position of the rigid body (User manual). Moreover, considering the multiple nested motions of a FOWL, the superposed technique was utilized to impose the rotational motion of the rotor onto the motion of a 6-DOF rigid body. All the models introduced in the present work were accomplished using the commercial software STAR-CCM+.

3.1.4. Computational domain

The current study was carried out employing an overset mesh approach to manage the intricate movement of a full-scale buoyant turbine. This mesh is utilized to discretize the computational flow region as shown in Fig. 5. Depending on the spatial arrangement of the cellular entities within the computational region, there is a potential to serve as passive, active or acceptor cells. The active cells that are used for the simulation are those whose governing fluid flow equations are solved within them. Passive cells are those cells that have no equations solved within them, while the acceptor cells are those that are located between active and inactive cells. Furthermore, there is a facilitated interpolation of the information between the overset and background meshes. In the present study, a fully structured mesh with trimmed cell hexahedrons were utilized. Since the VOF approach was employed to determine the location and format of the free surface wave. Consequently, appropriate local mesh techniques must be employed on the free wave. In this regard, the refinement pertaining to the undistributed free surface can be made by discretizing the free surface in this direction using nearly 10 to 30 cells per wave height. Moreover, the refinement parallel to the undistributed free surface can be applied by discretizing the free surface in this direction using nearly 80 to 120 cells per wavelength. Besides, dens mesh zones were adapted around the nacelle, blades, platform, and the tower to effectively estimate the flow characteristics and to enhance analysis reliability. To precisely encapsulate the properties of high gradient flow within the confines of the boundary layer region, prism layers (10) were generated adjacent to surfaces with cell growth ratio normal to the wall and first layer thickness of 1.2 and 0.3 mm, respectively. The entire computational domain comprises three finite volume regions namely; background region, overset region, and rotor region. Fig. 5 comprehensively explains the current mesh resolution across the entire computational region and various sectional perspectives.

3.2. Engineering tools FAST and OrcaFlex

The concept of floating wind turbines is a comparatively novel subject matter, and only a limited number of prototypes have been implemented recently. Thus, several numerical codes have been created to promote the development of the wind industry and to better grasp the dynamics of full-scale floating turbines. In the present work, two numerical tools based on potential flow theory called FAST and OrcaFlex were employed for full-scale floating turbine investigation and to validate the CFD results. FAST (Fatigue, Aerodynamics, Structures, and Turbulence) has been developed by National Renewable Energy Laboratory (NREL) (Jonkman et al., 2005). It is an open-source code that was created for estimating loads on land-based and fixed-bottom wind turbines. Then, it has been modified to permit the modeling of floating-foundation wind turbines. FAST code is a comprehensive numerical tool for modeling two and three-bladed wind turbines, where the aerodynamic forces, hydrodynamic loads, blade deflection, as well as tower motion can be determined. Furthermore, it is capable of modelling the mooring system using various modules such as a quasi-static model (MoorDyn), finite element based on mooring dynamic module (FEA Mooring), and multi-segmented mooring line module (MAP) (Masciola et al., 2014). On the other hand, OrcaFlex is a marine dynamic software package created by Orcina Ltd. It is a time and frequency-domain analysis code, which combines aerodynamic forces, hydrodynamic loads, and cable dynamics (Masciola et al., 2013). OrcaFlex code solves tension, bending, and torsion using a discrete lumped mass approach with a time-stepping scheme that can either be explicit or implicit (Ma et al., 2019). However, most of the numerical codes are relay on empirical equations and some correction factors such as, conventional Blade Element Momentum theory (BEM), to estimate the aerodynamic loads (Hansen et al., 2006; Hansen, 2000).

4. Results and discussion

This study introduces a high-fidelity CFD simulation of a full-scale NREL-5MW wind turbine situated on a semi-submersible floating platform, employing a DFBI approach. Floating wind turbines, distinct from traditional fixed-bottom turbines, are affixed to floating structures, enabling deployment in deeper waters where fixed structures are impractical. Additionally, these turbines operate in a combined aerodynamic and hydrodynamic environment, where forces on the turbine blades interact with forces on the floating platform. To ensure an accurate representation of the system's behavior, it is imperative to account for both aerodynamics and hydrodynamics. Therefore, validation of both aspects is essential for a comprehensive and precise CFD simulation of floating wind turbines. In light of the points mentioned earlier, this section introduces the validation process, encompassing aerodynamics with a focus on mesh sensitivity analysis, hydrodynamics verification involving hydrodynamic coefficients and free decay tests, and a fully-coupled simulation. Fig. 6 provides a concise overview of the entire methodology employed in this study.

4.1. Aerodynamic verification

This section involves both mesh indolence study and aerodynamic analysis of fixed-bottom wind turbine.

4.1.1. Mesh sensitivity test

The independence test was performed to ensure that mesh size is precise enough to effectively capture the aero-hydrodynamic responses and the outcomes obtained do not depend on the size of the spatial grid (Kim et al., 2019; Yang et al., 2023; Almola and Dawood, 2021; Hamdoon, 2020; Jasim et al., 2023). Grid sensitivity analysis was carried out by considering four arbitrary mesh densities, as shown in Table 2. The investigation was performed for a floating wind turbine under fixed-bottom conditions (the six degrees of the platform freedom motion were constrained) at a rated wind velocity and rotor speed of 11.4 m/s and 12.1 rpm, respectively. The aerodynamic torque and thrust force acting on the blades were adopted as the convergence criterion for

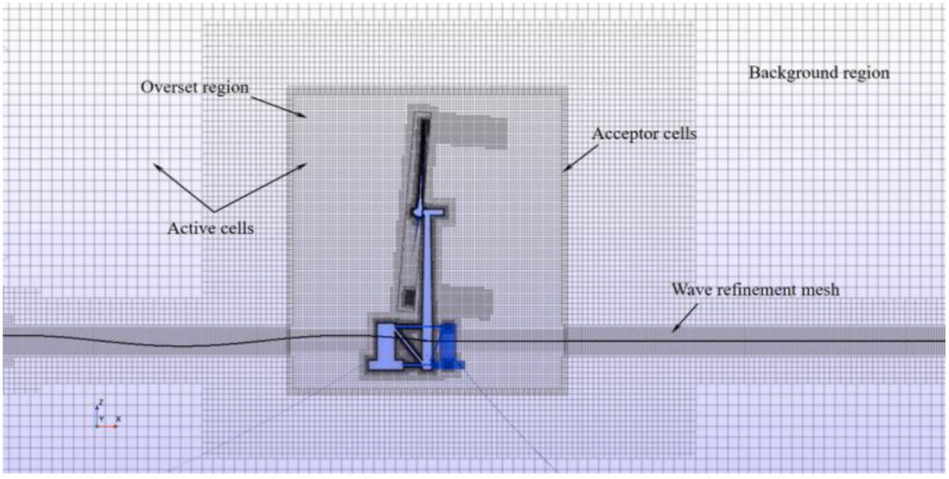

(a)

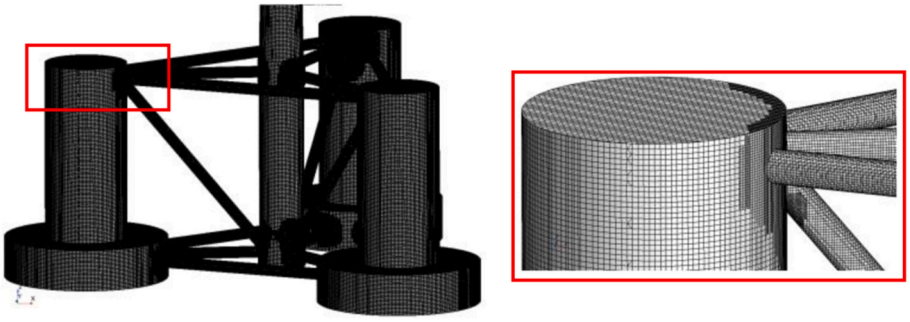

(b)

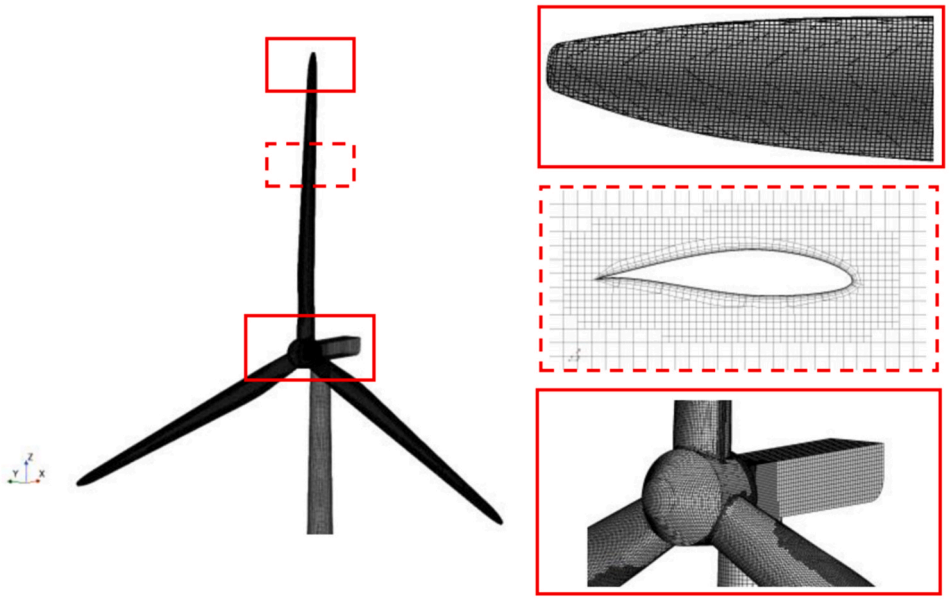

(c)

Fig. 5. The computational domain for full-scale FOWT: (a) cut slice of the entire domain, (b) close up view of the platform, (c) close up view of the rotor and nacelle.

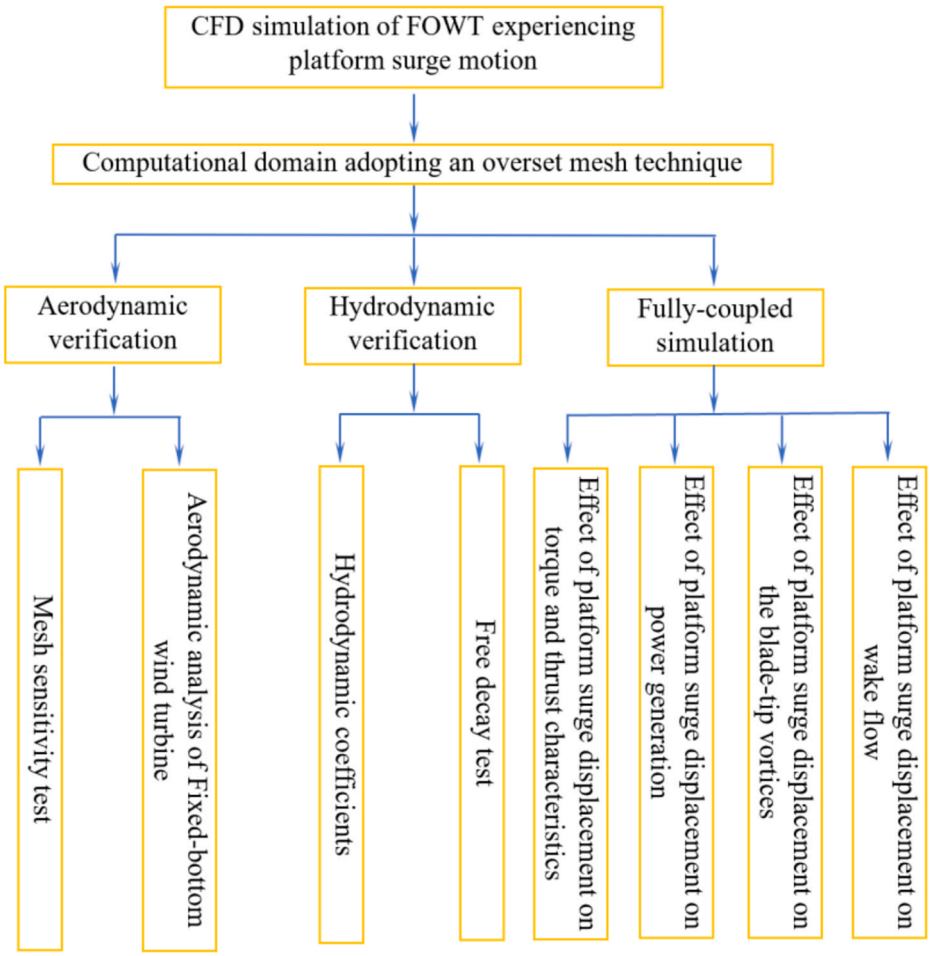

Fig. 6. Overview of the entire procedure implemented in this study.

Table 2
Mesh independence test at wind velocity of 11.4 m/s.

Mesh size	Base size	No. mesh	Torque (kN.m)	Error (%)	Thrust (kN)	Error (%)
Fine	0.2	26,421,136	4331.93	3.57	822.94	0.4
Medium	0.25	17, 210,041	4283.43	2.41	808.68	1.34
Coarse	0.3	12,288,931	4077.32	2.52	798.19	2.62
Ex. Coarse	0.35	10,968,631	3989.58	4.62	788.98	3.75
FAST			4182.7		819.7	
OrcaFlex			4227.1	1.06	826.16	0.79

selecting the proper mesh resolution.

Fig. 7 displays the time histories of both torque and thrust force obtained from CFD simulation for various mesh resolutions. Overall, an acceptable agreement was identified between CFD findings with those from FAST and OrcaFlex codes. According to the relative difference between various mesh densities based on FAST results, the medium mesh with a base size of 0.25 is sufficient enough to achieve simulation reliability. Thus, the grid with a resolution of 17, 210,041 mesh cells has been employed for the subsequent simulations.

An appropriate time step can be considered an important factor affecting CFD simulations. Based on the mesh size, wind speed, and the blade rotational speed, the time step must be sufficiently diminutive to apprehend the aerodynamic interference between the rotor wake, blade tip and supporting platform. Moreover, the time-step selection should consider the effect of hydrodynamic response, considering the wave conditions at rated rotor speed of 12.1 rpm (1.26 rad/s = 72.6 deg/s), the time it takes to complete one revolution of the blade is about 5 s. Taking into account the increment of the blade azimuth angle equals 2, the proper time-step used in the present CFD investigation is 0.0275 s.

4.1.2. *Aerodynamic analysis of fixed-bottom wind turbine*

As part of the verification step, the unsteady aerodynamic performance of a full-scale floating wind turbine was tested under fixed-bottom foundations. In this analysis, all platform hydrodynamic responses are restricted and set to an initial value of zero. To better grasp how the platform displacements affect the aerodynamic behavior of floating turbine, results obtained from this investigation will be compared with those from individual platform responses. Based on the selected mesh size, the simulation was carried out under various wind conditions. The angle of blade pitch is fixed at $(0°)$ when the incoming wind speed is lower than 11.4 m/s, while the blade pitch angle of 10.5° is adopted at 15 m/s to keep the speed of rotor fixed at 12.1 rpm.

As shown in Fig. 8 that unsteady aerodynamic performances take 4 revolutions to achieve a convergence state, the BEM solver of engineering tools uses a similar steady-state from the beginning of the simulation. It is observed that the effect of blade-tower interference was also taken into consideration. Overall, the time histories of power generation obtained from the present high-fidelity CFD simulations are in agreement with corresponding data from engineering tools; OrcaFlex and FAST. Interestingly, the aerodynamic power predicted by CFD simulation is slightly higher than those of engineering tools.

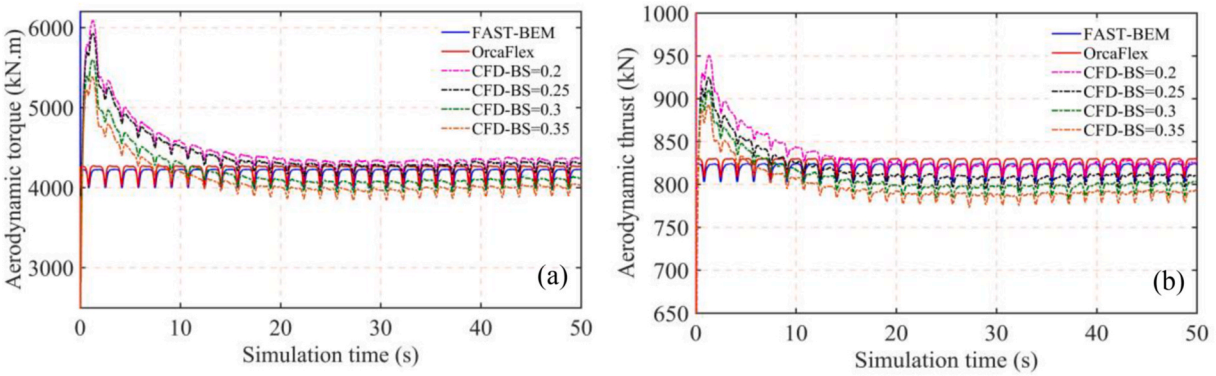

Fig. 7. Mesh sensitivity analysis of fixed-bottom wind turbine at wind speed of 11.4 m/s: (a) time histories of aerodynamic torque, (b) time histories of thrust force.

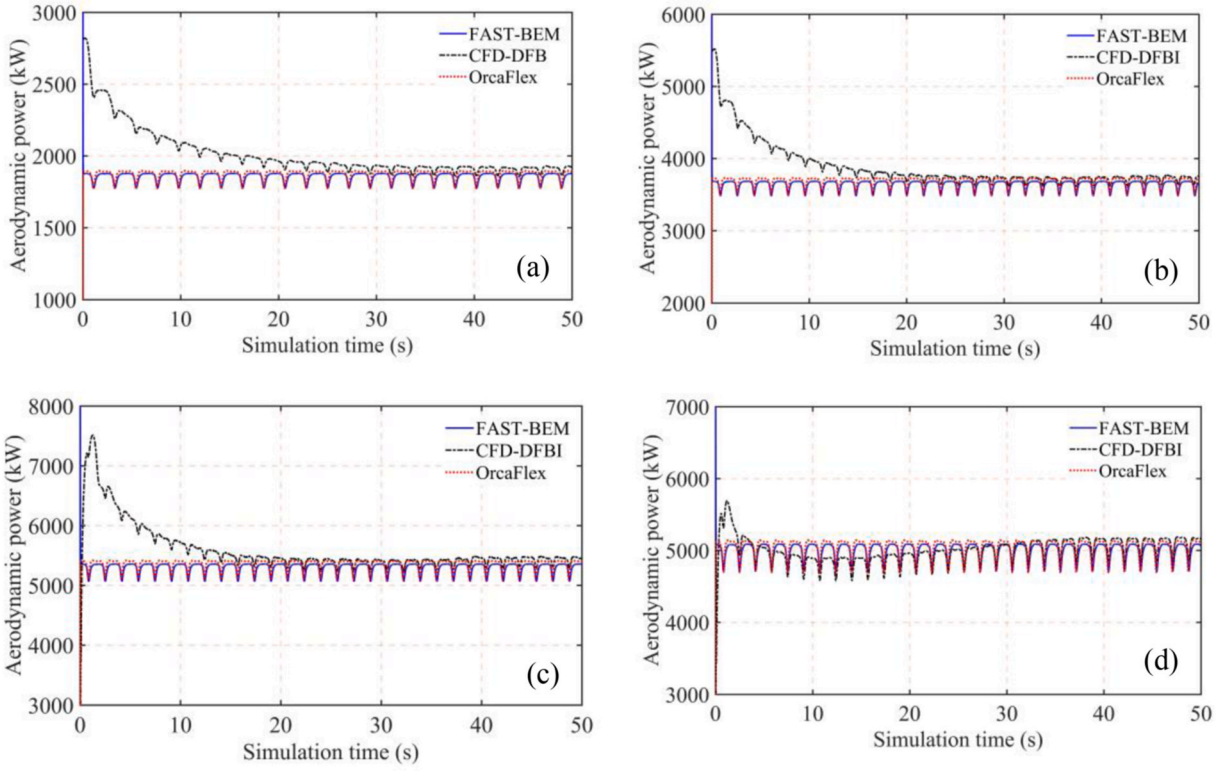

Fig. 8. Aerodynamic power for fixed-bottom wind turbine: (a) u = 8 m/s, (b) u = 10 m/s, (c) u = 11.4 m/s, (d) u = 15 m/s.

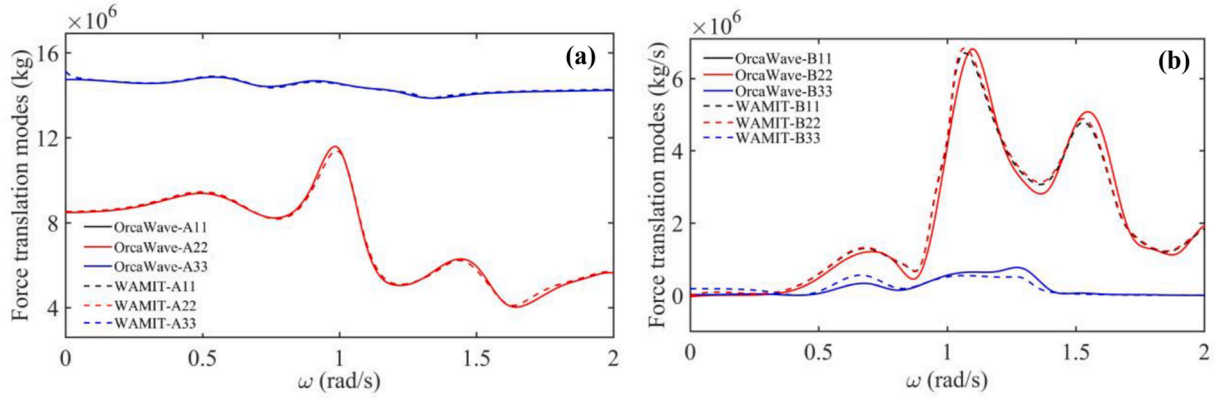

Fig. 9. Comparison of hydrodynamic properties: (a) added mass, (b) damping matrix for the semi-submersible platform.

4.2. Hydrodynamic verification

This section involves the analysis of hydrodynamic coefficients, free decay test, and the natural and damping coefficients.

4.2.1. Hydrodynamic coefficients

In order to accurately model the impact of aero-hydrodynamic-motion coupling for a full 5-MW floating offshore wind turbine. Accordingly, this study has done step-by-step verifications of standalone hydrodynamic and aerodynamic simulations. For the hydrodynamic verification study, a series of simulations using engineering tools including FAST and OrcaFlex was performed.

Fig. 9 presents the profile of diagonal translational added-mass and damping matrix between two probable solvers (OrcaWave and WAMIT), in which their hydrodynamic coefficients are inputted by OrcaFlex and FAST solvers, respectively. Overall, an excellent agreement is observed between both potential solvers. A small deviation, particularly for the heave damping coefficient between two codes, is observed. As they have different mesh resolutions, this small discrepancy at two frequency regimes is acceptable.

4.2.2. Free decay test

To further verify the accuracy of hydrodynamic simulation, the free decay analysis of OC4-Semisubmersible platform with three catenary lines was conducted. However, the structural properties (mass, mass moment of inertia, center of mass) of the full configuration floating wind turbine (blades, nacelle, tower, and platform) are considered in the simulation. Thus, the mass center (CG) of the full configuration was placed at 10.55 m below SWL in the z-direction and offset 0.01 upstream of the rotor due to the fully assembled model. Details of the structural characteristics of the considered wind turbine are reported in Table 3.

The free decay test was performed using the platform surge response. In this simulation, the platform was initially offset by 22m, and then released to its original theoretical equilibrium position in order to initiate a decay motion. The CFD simulation was performed for 500s using both DFBI and VOF approaches. A methodical comparison of the surge-free decay between the present CFD simulation and those of different codes was done as shown in Fig. 10. Overall, the time responses of free-decay analysis obtained from potential codes show similar attitudes to the corresponding CFD results, except for somewhat amplitude discrepancies at the first cycle. Moreover, a slight difference in phase-angle could be captured between CFD results and potential codes due to the existence of non-linear wave loads. For free-decay surge response, it can be observed that CFD results show a longer wave period than the potential codes i.e., the floating body needs a longer period of time to travel the same distance. The occurrence of this phenomenon can be ascribed to the impact of fluid viscosity, which is often disregarded when employing potential codes.

4.2.3. Natural frequency and damping coefficients

The natural frequency response is utilized to evaluate the dynamic profile of the entire floating system. One possible way to increase the stability of the floating system is by avoiding the resonance phenomenon between the turbine parts and wave frequencies. In this regard, the blades, tower-flexibility are normally designed with much higher natural frequencies than those of floating platform responses (Masciola et al., 2013). A comparison of natural period of a rigid body OC4-semisubmersible platform between numerical solutions and experiment data (Coulling et al., 2013) and CFD results (Tran and Kim, 2016a) is listed in Table 4.

4.3. Fully-coupled simulation

The turbine is coupled with the floater via a slightly tall cylindrical tower structure; therefore, the unsteady aerodynamic loads and hydrodynamic forces exert a substantial impact on the entire system stability and may cause a big aberration of the motion and vice versa. In this regard, the feedback mechanism between the aerodynamic performance of the rotor and the stability of its floating platform must be taken into account. Accordingly, the current work aims to investigate the influence of OC4-semisubmersible platform surge displacement on the aerodynamic performance of the NREL reference 5-MW wind turbine under fully-coupled wind-wave loads conditions. The hydrodynamic surge response is examined employing a high-fidelity CFD simulation relay on the DFBI approach. The current simulation was implemented at a rated wind speed of 11.4 m/s with fixed value of rotor speed at 12.1 rpm. According to the rotor speed, the time span to complete one blade revolution (360°) is around 5 s. The increment of the azimuth angle of the blade at each global time-step was assumed to be (2°) during the time marching iterations. Therefore, the size of the time step was selected to be 0.0275 s for the current simulation. The blade pitch angle of (0°) was fixed throughout the period of simulation. The environmental wave conditions persist consistently throughout the simulation, ensuring the maintenance of identical operating conditions across all the cases investigated. The investigation was performed under an extreme wave height of (7.58 m), whereas the wave period and water depth are 12.1s and 200 m, respectively. Moreover, the additional surge stiffness of 7.39 kN/m as a result of the impact of the cable bundle was considered as stated in Ref. (Coulling et al., 2013). Wind and wave heading angle of (0°) was adopted, which is parallel to the platform surge-motion. All properties and environmental conditions are listed in Table 5.

4.3.1. Effect of platform surge displacement on torque and thrust characteristics

The numerical investigation entails examining the hydrodynamic effect of the platform when it experiences surge displacement on both the aerodynamic behavior and wake properties of the reference NREL 5-MW wind turbine. This examination is conducted through the utilization of diverse simulation tools. To examine the impact of surge response, all platform displacements are restricted except the surge motion was released. The power output of the floating turbine under surge motion is compared with the main case. The main case represents the typical NREL 5-MW floating turbine under fixed-platform conditions, where all platform responses are kept constant at 0. Fig. 11 presents the historical time of the platform surge response for CFD outcomes and those of FAST and OrcaFlex. Generally, the findings exhibit a remarkable degree of similarity, albeit with subtle variations that can be discerned among the various codes. It is evident that the temporal records of the surge displacement exhibit a cyclic sinusoidal movement with oscillations at a consistent frequency matching that of the incoming wave. For a more

Table 3
Structural characteristics of the full configuration FOWT.

Part name	Mass	I_{xx}	I_{yy}	I_{zz}	X_{cg}	Y_{cg}	Z_{cg}
	kg	kg-m^2	kg-m^2	kg-m^2	m	m	m
RNA	3.5000E+05	2.8515E+09	2.8314E+09	2.5480E+07	−0.41	0	89.56
Tower	3.0206E+05	7.5033E+08	7.5033E+08	2.0160E+06	0	0	44.64
Platform	1.3444E+07	1.0799E+10	1.0799E+10	1.3910E+10	0	0	−14.4
Full FOWT	1.4096E+07	1.4401E+10	1.4380E+10	1.3937E+10	−0.01	0	−10.55

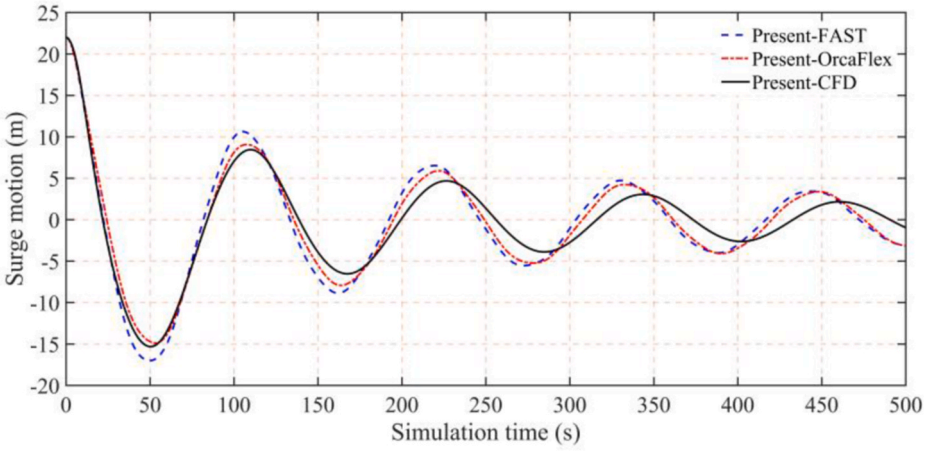

Fig. 10. Comparison of surge free-decay responses of the semi-submersible.

Table 4
A comparison of natural periods of a rigid-body OC4 DeepCWind platform under surge response.

	Tool	Period (s)	Frequency (Hz)
(Coulling et al., 2013)	Exp.	107	9.3E-3
	FAST	107	9.3E-3
Tran and Kim (2016a)	FAST	120	5.0E-1
	CFD	108.1	9.2E-3
Present work	OrcaFlex	114.2	8.7E-3
	FAST	111.08	9.0E-3
	CFD	116.2	8.6E-3

Table 5
Environmental and operating conditions.

Parameter	Value	Unit
Wind velocity	11.4	ms^{-1}
Current velocity	0	ms^{-1}
Rotor speed	12.1	*rpm*
Wave height	7.58	*m*
Wave period	12.1	*s*
Water depth	200	*m*
Wave model	First-order regular model	
Blade pith angle	0°	
Wind/Wave heading angle	0°	
Air density	1.225	kgm^{-3}
Water density	1025	kgm^{-3}

comprehensive understanding and analysis (refer to Fig. 11 zoom-in view), a specific timeframe within the CFD simulation time histories (400s–425s) was considered. It is noted that the average value of the platform surge response obtained from CFD investigation closely aligns with those values from FAST and OrcaFlex, although there are some differences in the amplitudes. It is observed that the average value obtained from CFD simulation was approximately 9.79 m with an absolute difference of 8.7 % and 5.31 % compared to both FAST and OrcaFlex, respectively. Moreover, the maximum amplitude of an oscillating surge response estimated by CFD approach was approximately 12.26 m with a slight difference of 6.98 % and 3.67 % from FAST and Orcaflex, respectively. For more details, the maximum, minimum, and average values of the platform surge response are summarized in Table 6.

To test the aerodynamic properties of the wind turbine under the surge displacement effect, Fig. 12 and Fig. 13 illustrate the historical time of the aerodynamic torque and thrust obtained from the CFD approach and potential codes FAST and OrcaFlex. It is observed that aerodynamic torque and thrust are time-dependent due to the floater surge response, where an oscillating sinusoidal motion describes the variation of both torque and thrust curves. The aerodynamic torque obtained from different numerical tools are quite consistent with regard to the phase angle and amplitudes as depicted in Fig. 12. The average rotor aerodynamic torque obtained from CFD approach is 4241 kN m with a slight variation of 0.47 % and 5.16 % compared to corresponding data from FAST and OrcaFlex, respectively. For a more comprehensive understanding and analysis (refer to the zoom-in view in Fig. 12), torque time histories during a specific timeframe (400s-425 s) were taken into consideration. It is disclosed that the maximum value of aerodynamic torque obtained from the CFD simulation during the period (400s–425s) was determined as 5581 kN m, showing differences of approximately 0.97 % and 4.79 % compared to the values from both potential codes as illustrated in Table 6.

The time histories of aerodynamic thrust closely resemble the torque curves, with the exception of some variations in phase amplitudes observed between different numerical tools, as illustrated in Fig. 13. Overall, the aerodynamic thrust obtained from CFD approach is lower than that estimated by potential codes FAST and OrcaFlex. The average aerodynamic thrust by CFD method is approximately 10.2 % and 4.57 % less than the corresponding data from FAST and OrcaFlex, respectively. Moreover, the maximum amplitude of aerodynamic thrust from CFD simulation is less than that of FAST and OrcaFlex by approximately 11.4 % and 5.1 %, respectively. In the present study, the CFD analysis with an overset mesh technique is based on the DFBI approach, which is particularly used to simulate the motion of a rigid body in response to the fluid forces, moments, and gravitational forces. Furthermore, the viscous flow separation, tower-vortex shedding, the complex interactions between the blade-tip vortex and the wake flow due to the platform motion are directly considered in the CFD simulation. On the other hand, the conventional BEM method based on the potential flow theory was applied in both FAST and OrcaFlex codes. Thereby, these codes cannot adequately capture the impacts of the unsteady flow phenomena around the rotating blades. Moreover, the relative velocity of the floating structures (blades, hub, nacelle, and the tower) induced by the platform-surge motion is not included in the BEM approach. In addition, aerodynamic coefficients are utilized in FAST and OrcaFlex to estimate the complex interference between the blade-tip vortices and its own wake when the turbine moves backward due to the platform oscillating motion.

In addition to the impact of platform displacement, the tower shadow exerts a notable influence on the unsteady torque and thrust behavior. Observable sudden drops occur in the aerodynamic torque and thrust curves, indicating instances of blade-tower interference. This phenomenon occurs as the rotor blades sequentially pass by the tower. Within a 5-s timeframe encompassing one complete revolution, three

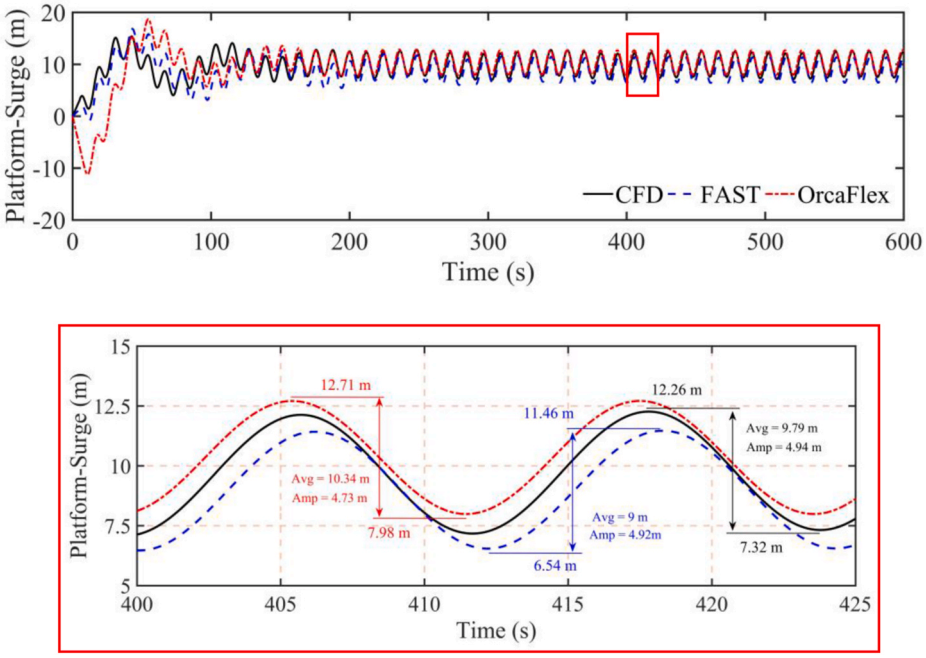

Fig. 11. Profiles of the historical time of the platform-surge response for various codes.

Table 6
Comparison of surge response and aerodynamic factors between different numerical tools.

	CFD			FAST			OrcaFlex		
	Max	Min	Mean	Max	Min	Mean	Max	Min	Mean
Surge (m)	12.26	7.32	9.79	11.46	6.54	9	12.71	7.98	10.34
Error (%)				6.98	11.9	8.7	3.67	8.27	5.31
Torque (kN.m)	5581	2901	4241	5636	2807	4221	5862	3083	4472
Error (%)				0.97	3.34	0.47	4.79	5.9	5.16
Thrust (kN)	837.1	626.2	731.6	945.2	685.6	815.4	883	650.4	766.7
Error (%)				11.4	8.6	10.2	5.1	3.72	4.57

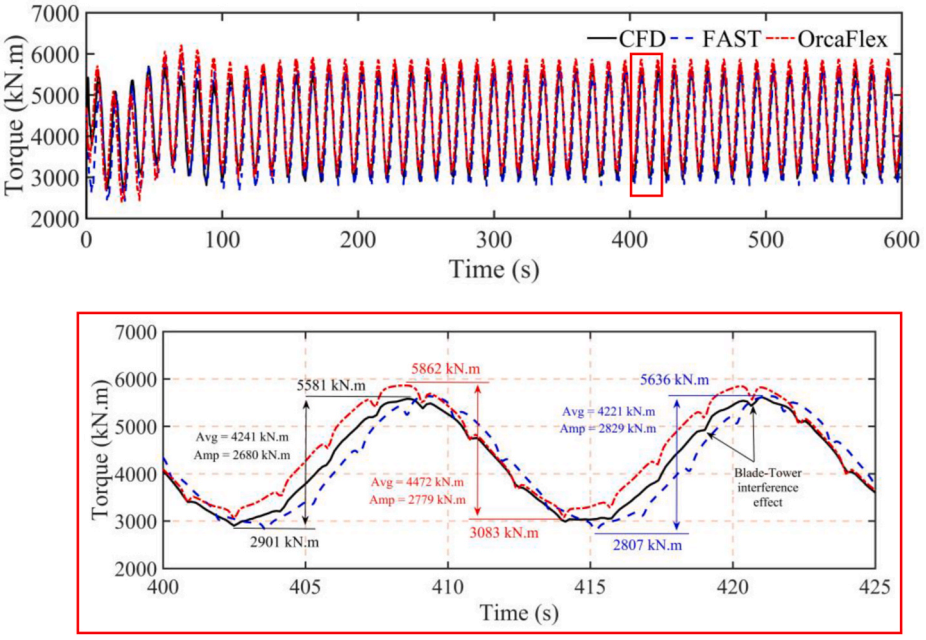

Fig. 12. Comparison of historical time of the aerodynamic torque.

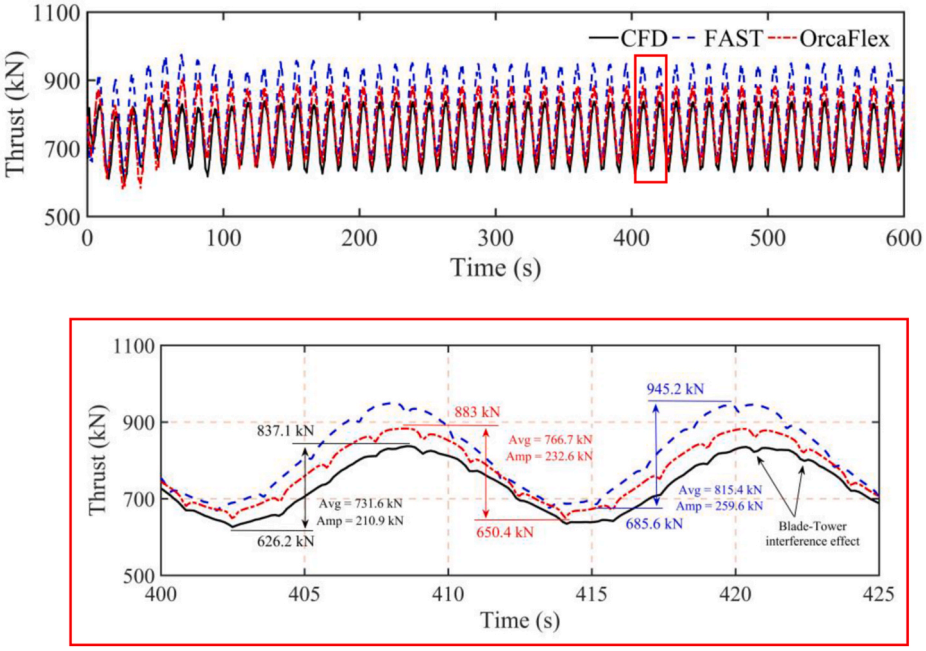

Fig. 13. Comparison of time histories of aerodynamic thrust.

blade-tower interferences take place when the three blades pass in front of the tower. Consequently, three sudden local minima are evident along the torque and thrust curves during each cycle. Refer to Figs. 12 and 13 for visual representation of the blade-tower interference effect.

4.3.2. Effect of platform surge displacement on power generation

To gain a more profound understanding of the relationship between floater motion and aerodynamic characteristics in terms of power gains or losses, it is essential to analyze the relation between the platform displacement and its linear velocity, power generation, and the inflow wind velocity. Fig. 14 illustrates the partial time histories of the platform surge displacement and its corresponding linear velocity. Positions (A-E) represent one periodic cycle of the floater surge motion (two rotor revolutions).

It is observed that the platform experiences backward motion (displacement increases) during the period (A-C), where the movement of the object is co-directional with the velocity of the incoming wind. Contrarily, the platform is subjected to forward motion (displacement decreases) for the positions (C-E), where the movement of the object occurs in a contrary direction to the oncoming air current. It is observable that the platform achieves its utmost forward position and backward displacements at positions (A and C), where the linear surge velocity reaches its minimum values at these positions. Moreover, the maximum surge velocity is obtained when the platform returns back from its maximum displacements (A and C) to its initial positions (B and D). Moreover, the platform surge motion affects the apparent wind velocity normal to the rotor plane. When the turbine experiences surge motion, the apparent wind velocity is the superposition of the incoming wind velocity and the surge induced-velocity as stated in Fig. 15.

The related wind velocity applied to the rotor plane of floating wind turbine can be described using this formula:

$$u_{rel} = u_o + u_s \tag{3}$$

$$u_s = \left(\frac{2\pi A}{T}\right) sin\left(\frac{2\pi}{T}t\right) \tag{4}$$

Where u_{rel} is the relating wind speed, it is the superposition of incoming wind velocity u_o and the surge-induced velocity u_s. The A and T are the wave amplitude and wave period respectively. The variation of wind velocity caused by the platform surge motion is depicted in Fig. 16.

Fig. 17 displays the relation between the power generation and the relative velocity. Due to the cyclic motion of the floating turbine, the power output fluctuates within the same cycle as the surge

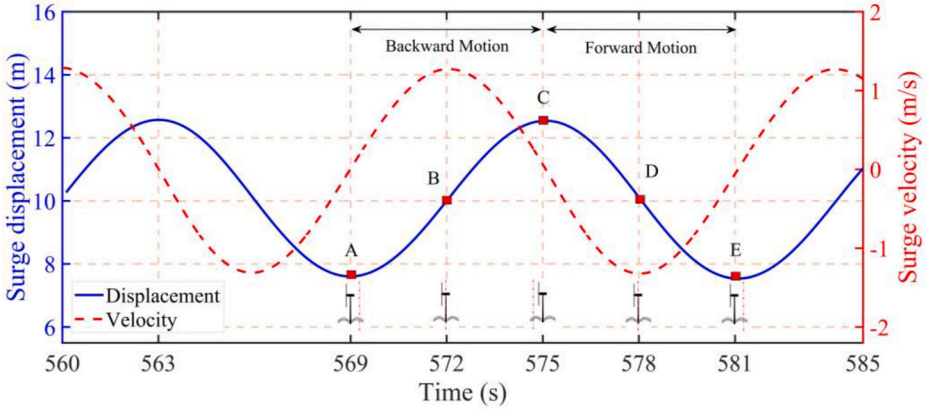

Fig. 14. Correlation between surge displacement and the platform velocity.

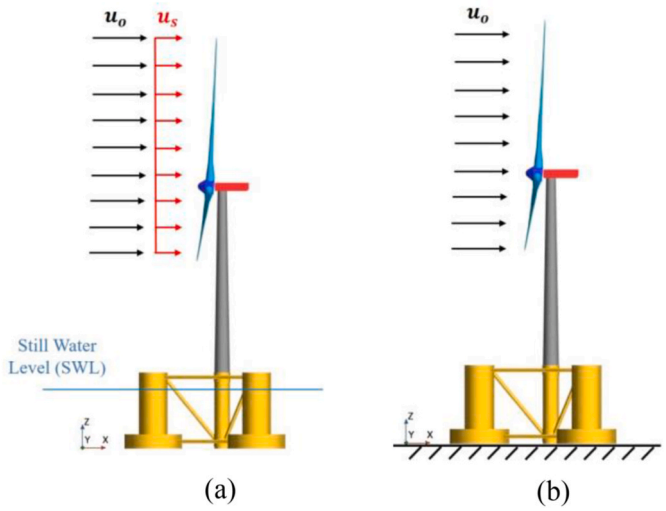

Fig. 15. Distribution of velocity on the rotor: (a) floating turbine under surge displacement, (b) fixed-bottom turbine.

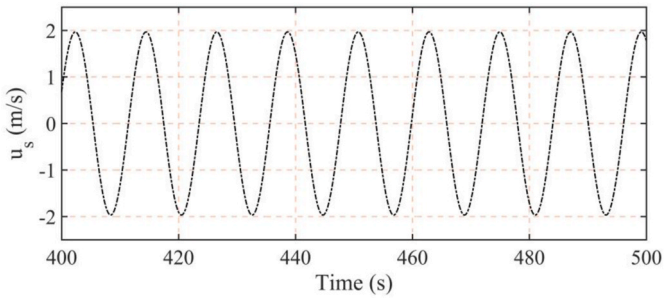

Fig. 16. Historical time of the surge-induced velocity.

displacement. The power generation under periodic surge motion fluctuates around the corresponding power obtained from the fixed-bottom turbine. When the floating turbine surges backward (A-C), the relative velocity normal to the rotor plane decreases, thereby, reaching its minimum value at position (B). With a decrease in relative wind velocity, the power generation is also predicted to decrease in comparison with that of a fixed bottom wind turbine. In contrast, when the floating turbine experiences forward motion (C-E), the relative wind speed increases to its maximum value at position (D). Accordingly, due to the increase in relative wind speed, the amount of generated power from floating turbines rises in comparison with that of fixed bottom turbines (see Fig. 18).

4.3.3. *Effect of surge displacement on the blade-tip vortices*

This section discusses the impact of the platform surge displacement on the unsteady flow behavior near the blade-tip region and the complex interactions between the blade-tip vortices and the downward wake flow. Fig. 18 depicts a numerical visualization using iso-vorticity contours of the blade-tip interactions. To highlight the influence of surge displacement on the rotor wake interactions, a comparison of instantaneous blade-tip vorticity between the turbine under surge displacement effect and the fixed-bottom turbine was made. For the surge period (A-C), the turbine experiences backward motion, whereas in the period (C-E), the turbine takes a forward motion. Overall, complex shedding vortices from different turbine components like blade-tip, nacelle, tower and hub are observed. It is observed that the blade-tip vortices are formed into individual helical rings and deployed in the wake downstream of the rotor. However, the blade-tip helical tubes are highly affected by the platform surge displacement in comparison with those produced from fixed-bottom turbines. As the floating turbine takes a backward motion (A-C), the rotor moves into its own wake causing complex interaction between the blade-tip vortices and the wake flow. In this regard, the gap distance between the tubes obtained from blade-1 and blade-2 decreases, and the number of helical rings increases. In contrast, as the turbine experiences forward surge motion (C-E), the rotor moves out of its own wake, which ultimately diminishes the aerodynamic interference between the blade-tip vortices and the wake flow. Moreover, the number of helical rings decreases and the gap space among the helical rings increases. Compared with the fixed-bottom turbine, the individual helical tubes obtained from different blade tips are pretty similar and have the same specifications. Thus, the number of helical rings and the gap space among them remain unchanged over time.

4.3.4. *Effect of surge displacement on wake flow*

Operating wind turbines educe kinetic energy from the up-flow wind. However, rotating blades can generate velocity deficit behind the rotor disk and also huge turbulence. These vortices coalesce into a vortex sheet of the blade and are shed in the wake downstream of the rotor. These vortices travel downstream the rotor until they are diffused. In a wind farm, these sheets coalesce in a system of vortices that exchange energy with the upper part of the atmospheric boundary layer. These massive systems of vortices can interact in clusters of wind farms, thereby modifying the local wind climate. Thus, the wake study is very important not only for turbine designers but also for wind farm developers for the optimization of layout turbines in wind farm array. Fig. 19 compares the iso-vorticity contours of the floating wind turbine under platform surge response with that under a fixed-bottom turbine at steady state condition. It is evident that both the tip and root of the blade

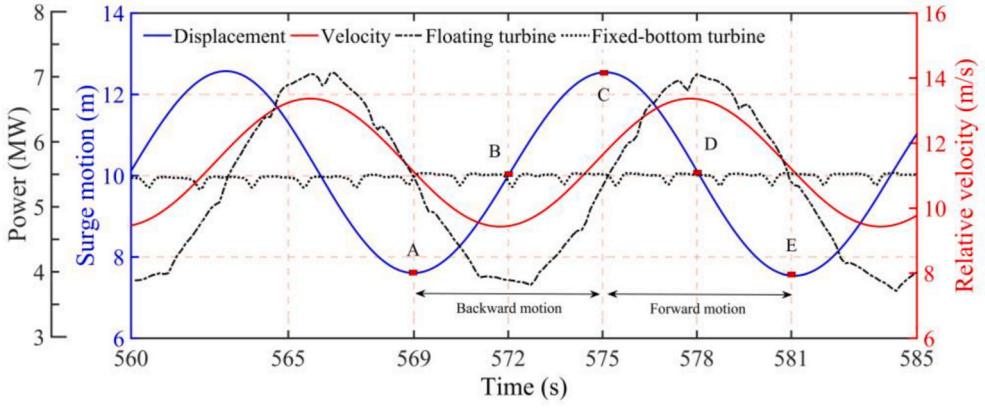

Fig. 17. Relation between power generation and relative velocity.

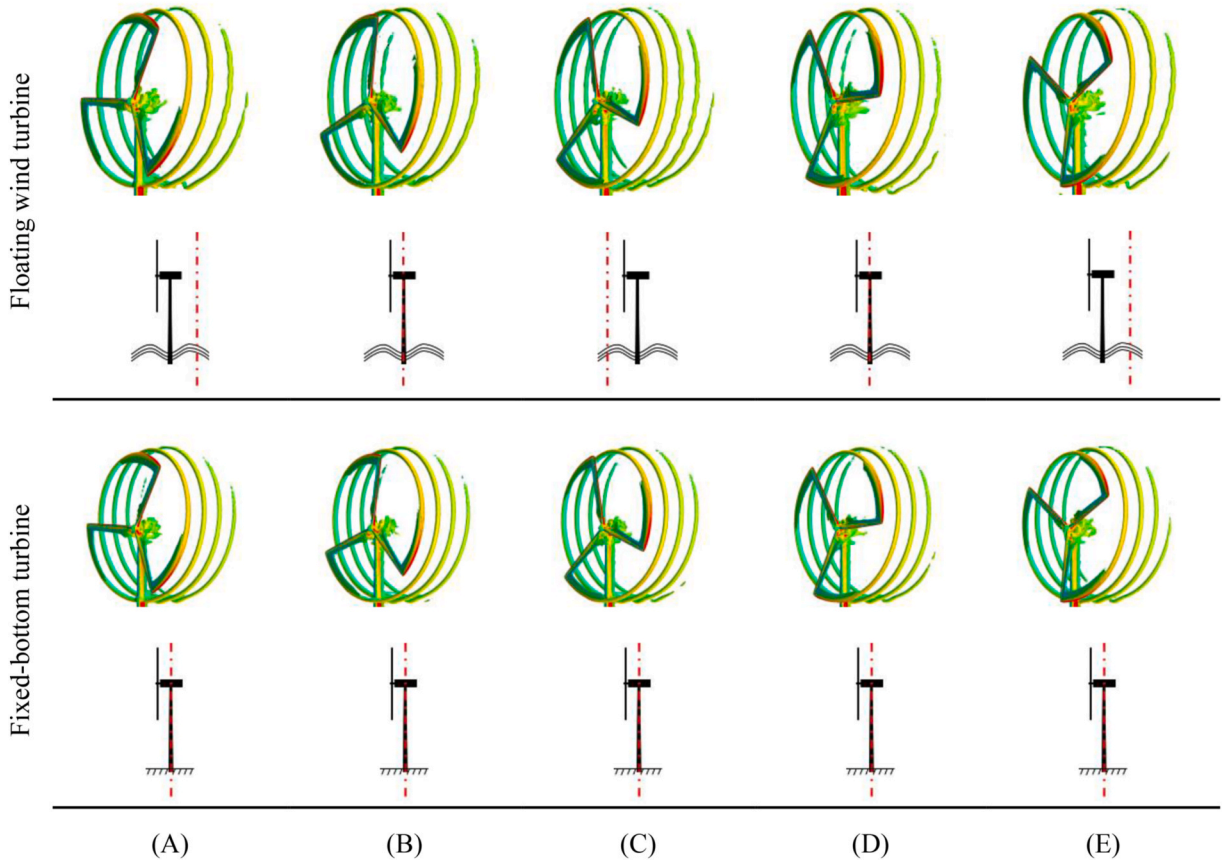

Fig. 18. Comparison of instantaneous blade-tip vortices between floating turbine under surge displacement and fixed-bottom turbine.

generate vortices and huge turbulence downstream of the rotor. Moreover, the blade tip vortices are faster and stronger than those from the blade root. Thus, the blade tip vortices extend to a longer distance downstream of the rotor than those from the blade root. It is observed that both tip and root vortices under surge motion travel to a certain distance and then scatter into discrete eddies in the far wake downstream of the rotor. In contrast, the tip and root vortices under fixed platform conditions are uniformly travelled downstream of the rotor with less scattered eddies. Consequently, wake flow downstream of the rotor under surge motion is more turbulent than that under fixed platform conditions, which suppress the velocity deficit by bringing air into the wake region and recovering the velocity in it.

Fig. 20 depicts the top view of axial velocity contours for both the rotor subjected to the surge motion and the one under fixed platform conditions. Overall, the wind turbine rotor disturbs the incoming wind flow. Thus, downstream of the rotor, the wind velocity profile is substantially modified. The velocity deficit that arises from the exertion of force by the rotor results in a notable decrease in the wind speed. Placing an additional wind turbine within this region of wind turbulence will result in a diminished velocity of the incoming wind, subsequently leading to a decrease in power generation. It is observed that there are gradients of the velocity in the profile, especially at the bottom and top of the rotor. These shear layers are the source of vortex generation, meaning that turbulent eddies are shed in the wake. As the rotor under surge displacement moves in and out on its own, it causes complex aerodynamic interactions between the blade helical tubes and the wake downstream of the rotor, which eventually generates more discrete eddies downstream of the rotor than those from the turbine under fixed platform condition as seen in Fig. 19. These vortices tend to suppress the velocity deficit by bringing air from outside the deficit region into the deficit region. In addition, as the turbine under surge motion oscillates about its neutral position, the platform surge motion inspires the apparent wind velocity perpendicular to the rotor plane. Therefore, the rotor under surge displacement captures more energy compared to that under fixed platform conditions. Consequently, it is detected that the velocity recovery downstream of the rotor under surge displacement is faster than that of the rotor under a fixed platform, specifically in the far wake zone. To highlight the velocity recovery process, Fig. 21 illustrates the normalized velocity profile at different locations downstream of the rotor for both turbines. Overall, as the distance downstream the rotor increases, the velocity recovery of the fixed turbine slows down compared to that of the floating turbine. As it is observed in Fig. 21(a), the gap distance between the velocity profiles of both turbines is close, indicating that the velocity recovery process takes approximately the same time to achieve. In contrast, the difference between the velocity profiles of both turbines increases at a distance of 7D downstream of the rotor as illustrated in Fig. 21(d), indicating that the velocity recovery process of the floating turbine is faster than that of the fixed turbine. Hence, in the wind farm, the turbines under surge motion can be placed in an array closer to each other compared to the corresponding turbines under fixed platform conditions. However, the process of wake recovery may require traversing a span equivalent to multiple turbine diameters prior to attaining complete wake restoration. In general, the optimal positioning of the turbine is achieved by finding a balance between the amount of power generated and the surface area of land required for its installation.

5. Conclusions

In this study, the numerical analysis of the influence of platform surge response on the aerodynamic behavior and wake properties of the floating wind turbine was conducted using high-fidelity CFD simulation. To gain a deeper understanding of the influence of platform surge response, the aerodynamic parameters in terms of power generation and

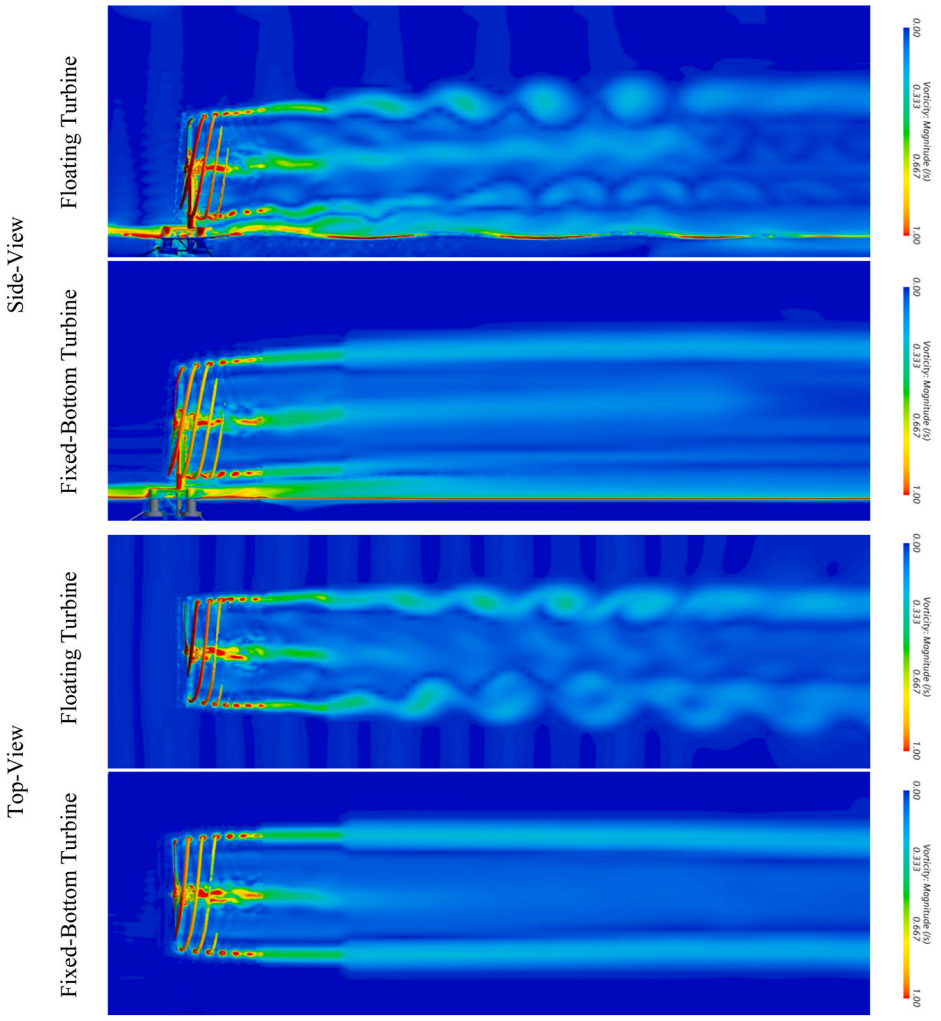

Fig. 19. Comparison of the iso-Vorticity contours between the floating turbine under surge response and fixed-bottom turbine.

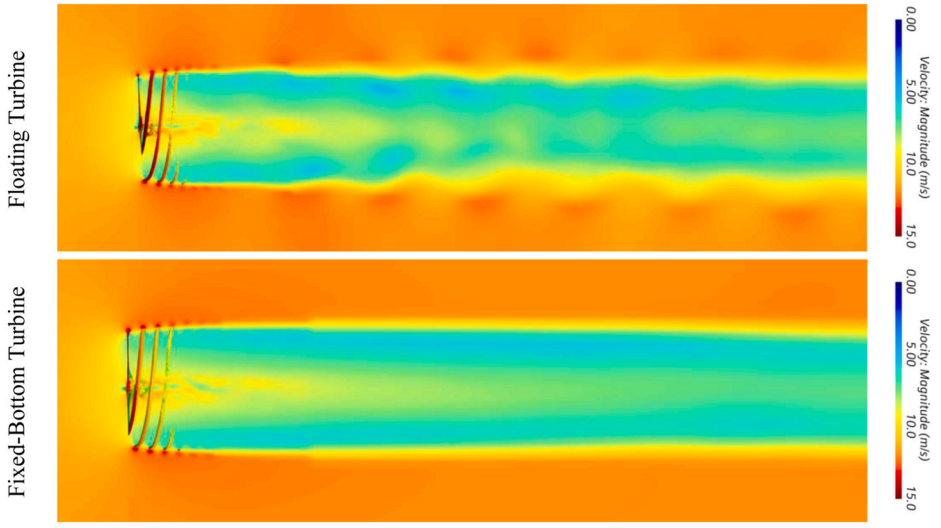

Fig. 20. The top-view of the axial velocity contours for both floating turbine under surge response and fixed-bottom turbine.

thrust force during the platform surge response are compared with the reference case. It involves a typical floating turbine under fixed-platform conditions, where all platform displacements are maintained constant at 0. This simulation employs an overset mesh technique to accurately capture the impact of the semi-submersible platform's surge response on both the aerodynamic behavior and wake properties of the 5-MW Floating Offshore Wind Turbine (FOWT). Furthermore, the integration of DFBI and VOF approaches is utilized to precisely understand the aero-

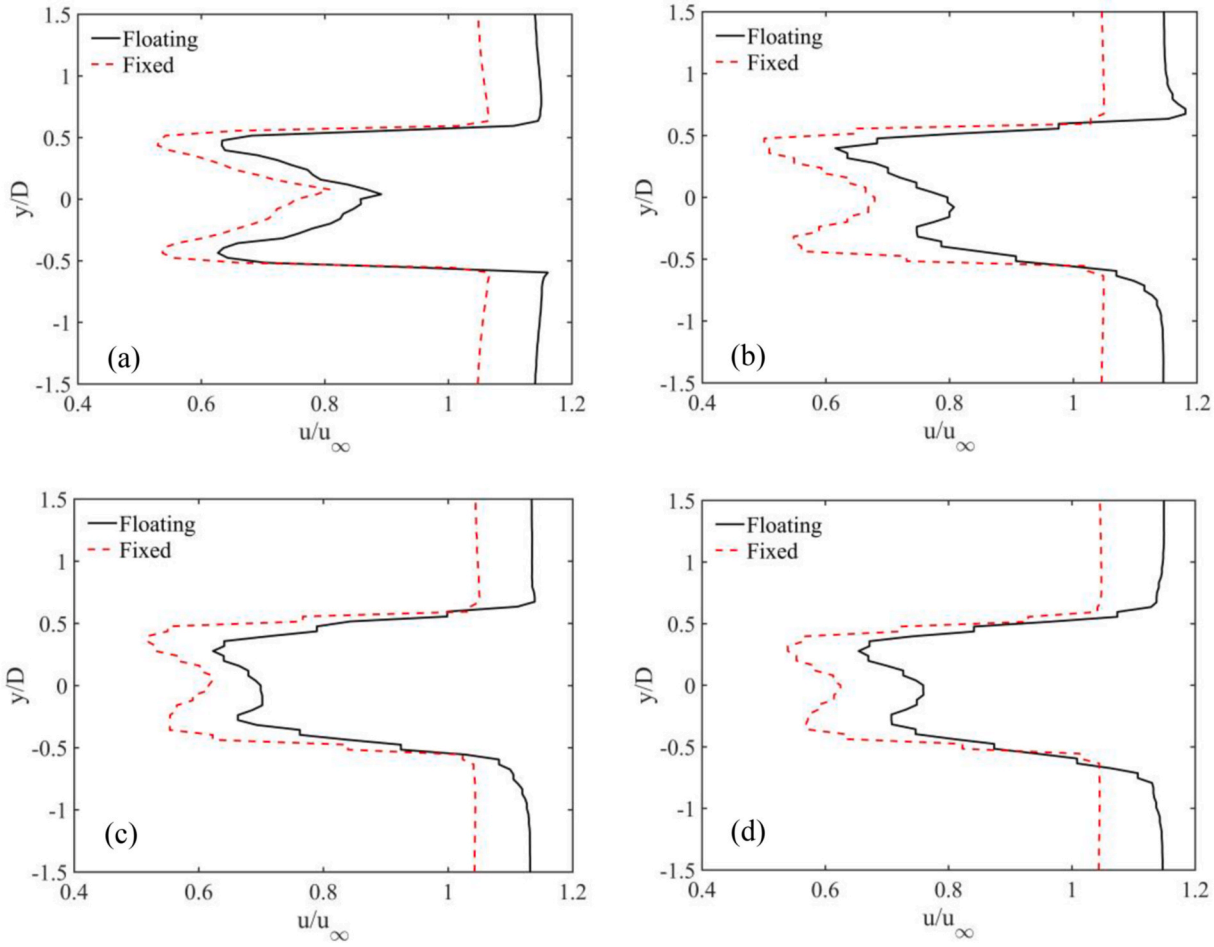

Fig. 21. Normalized velocity profile at different locations downstream of the rotor at the hub height plane: (a) 1D, (b) 3D, (c) 5D, (d) 7D.

hydrodynamic interaction and simulate the water-air interface surface. The CFD investigation was performed at a rated wind speed of 11.4 m/s, and extreme regular wave height of 7.58m. A systematic comparison of aerodynamic performance, hydrodynamic responses, and the catenary analysis results between CFD simulation and those of FAST and OrcaFlex based on the BEM model adapted. The CFD findings reveal a substantial effect of the platform surge response on the apparent wind velocity perpendicular to the rotor plane. This effect arises from the superposition of the incoming wind velocity and the surge-induced velocity. Hence, the power extracted from the rotor experiences fluctuations in surge motion within the same time frame as the surge displacement. Comparing the aerodynamic performance of a turbine subjected to surge displacement with that of a fixed-bottom turbine, the power generation under periodic surge motion fluctuates around the corresponding power obtained from the fixed-bottom turbine. Furthermore, a pronounced aerodynamic interference between the helical tubes at the blade tip and the wake flow was observed. Therefore, the wake flow downstream of the rotor during surge response exhibits higher turbulence compared to that of the stationary wind turbine. In this regard, the velocity recovery of the wake flow downstream of the rotor during surge motion is faster than that of the fixed-bottom turbine. Adequate spacing is crucial to optimize the efficiency of each turbine in a wind farm. Insufficient spacing may lead to interference in the wake of one turbine affecting the performance of the turbines located downstream. In conclusion, the point emphasizes that turbines with surge motion can be placed closer together compared to fixed turbines within a wind farm, and this is essential to minimize wake interference and optimize the overall efficiency of the wind farm. In future work, the platform surge response will be examined under various operating conditions, different values of wave heights and wind velocities, wind-wave heading angles, and current speeds.

CRediT authorship contribution statement

Ali Alkhabbaz: Writing – original draft, Visualization, Software, Methodology, Conceptualization. **Hudhaifa Hamza:** Validation, Methodology. **Ahmed M. Daabo:** Investigation. **Ho-Seong Yang:** Visualization, Software. **Min Yoon:** Conceptualization. **Aisha Koprulu:** Resources. **Young-Ho Lee:** Supervision, Conceptualization.

Declaration of competing interest

The authors declare that they have no known competing financial interests or personal relationships that could have appeared to influence the work reported in this paper.

Data availability

No data was used for the research described in the article.

References

Alkhabbaz, A., Yang, H.-S., Weerakoon, A.H.S., Lee, Y.-H., 2021. A novel linearization approach of chord and twist angle distribution for 10 kW horizontal axis wind turbine. Renew. Energy 178, 1398–1420. https://doi.org/10.1016/j.renene.2021.06.077.

Alkhabbaz, A., Yang, H.-S., Tongphong, W., Lee, Y.-H., 2022. Impact of compact diffuser shroud on wind turbine aerodynamic performance: CFD and experimental investigations. Int. J. Mech. Sci. 216, 106978 https://doi.org/10.1016/j.ijmecsci.2021.106978.

Almola, H., Dawood, A., 2021. Conjugate Heat Transfer of Nanofluid flow inside A micro– Wavy channel. Al-Rafidain Engineering Journal (AREJ) 26, 201–210. https://doi.org/10.33899/rengj.2021.129169.1078.
Arany, L., Bhattacharya, S., 2018. Simplified load estimation and sizing of suction anchors for spar buoy type floating offshore wind turbines. Ocean Eng. 159, 348–357. https://doi.org/10.1016/j.oceaneng.2018.04.013.
Aristodemo, F., Tomasicchio, G.R., Veltri, P., 2011. New model to determine forces at on-bottom slender pipelines. Coast Eng. 58, 267–280. https://doi.org/10.1016/j.coastaleng.2010.11.004.
Bagherian, V., Salehi, M., Mahzoon, M., 2021. Rigid multibody dynamic modeling for a semi-submersible wind turbine. Energy Convers. Manag. 244, 114399 https://doi.org/10.1016/j.enconman.2021.114399.
Balog, I., Ruti, P.M., Tobin, I., Armenio, V., Vautard, R., 2016. A numerical approach for planning offshore wind farms from regional to local scales over the Mediterranean. Renew. Energy 85, 395–405. https://doi.org/10.1016/j.renene.2015.06.038.
Benitz, M., Schmidt, D., Lackner, M., Stewart, G., Jonkman, J., Robertson, A., 2014. Comparison of Hydrodynamic Load Predictions between Engineering Models and Computational Fluid Dynamics for the OC4-DeepCwind Semi-submersible. NREL/CP-5000-61-61157.
Benitz, M., Schmidt, D., Lackner, M., Stewart, G., Jonkman, J., Robertson, A., 2015. Validation of Hydrodynamic Load Models Using CFD for the OC4-DeepCwind Semisubmersible. NREL/CP-5000-63751.
Beyer, F., Arnold, M., Cheng, P., 2013. Analysis of Floating Offshore Wind Turbine Hydrodynamics Using Coupled CFD and Multibody Methods. Int. Society of Offshore and Polar Engineers, pp. 261–267.
Butterfield, S., Musial, W., Jonkman, J., Sclavounos, P., 2007. Engineering Challenges for Floating Offshore Wind Turbines. Conference paper, NREL/CP-500-38776.
Carlson, D.W., Modarres-Sadeghi, Y., 2018. Vortex-induced vibration of spar platforms for floating offshore wind turbines. Wind Energy 21, 1169–1176. https://doi.org/10.1002/we.2221.
Castro-Santos, L., Diaz-Casaa, V., 2016. Flaoting Offshore Wind Farms. Springer.
Chen, P., Chen, J., Hu, Z., 2020. Review of experimental-numerical methodologies and challenges for floating offshore wind turbines. J. Mar. Sci. Appl. 19, 339–361. https://doi.org/10.1007/s11804-020-00165-z.
Chow, J.H., Ng, E.Y.K., Srikanth, N., 2019. Numerical study of the dynamic response of a wind turbine on a tension leg platform with a coupled partitioned six degree-of-freedom rigid body motion solver. Ocean Eng. 172, 575–582. https://doi.org/10.1016/j.oceaneng.2018.12.040.
Chuang, Z., Liu, S., Lu, Y., 2020. Influence of second order wave excitation loads on coupled response of an offshore floating wind turbine. Int. J. Nav. Archit. Ocean Eng. 12, 367–375. https://doi.org/10.1016/j.ijnaoe.2020.01.003.
Contestabile, P., Iuppa, C., Di Lauro, E., Cavallaro, L., Andersen, T.L., Vicinanza, D., 2017. Wave loadings acting on innovative rubble mound breakwater for overtopping wave energy conversion. Coast Eng. 122, 60–74. https://doi.org/10.1016/j.coastaleng.2017.02.001.
Coulling, A.J., Goupee, A.J., Robertson, A.N., Jonkman, J.M., Dagher, H.J., 2013. Validation of a FAST semi-submersible floating wind turbine numerical model with DeepCwind test data. J. Renew. Sustain. Energy 5. https://doi.org/10.1063/1.4796197.
G.W.E. Council, Global wind report 2021-annual market update. https://gwec.net/global-wind-report-2021.
Daabo, A.M., Hammo, K.E., Mohammed, O.A., Hassan, A.A., Lattimore, T., 2020a. Performance investigation and design optimization of micro scale compressed air axial turbine for domestic solar powered Brayton cycle. Sustain. Energy Technol. Assessments 37, 100583. https://doi.org/10.1016/j.seta.2019.100583.
Daabo, A.M., Bellos, E., Pavlovic, S., Bashir, M.A., Mahmoud, S., Al-Dadah, R.K., 2020b. Characterization of a micro thermal cavity receiver – experimental and analytical investigation. Therm. Sci. Eng. Prog. 18, 100554 https://doi.org/10.1016/j.tsep.2020.100554.
Diaconu, S., 2013. Wave Run-Up Simulations and Comparison with Experimental Data on a Semi-submersible, vol. 1, pp. 32–37.
Duan, F., Hu, Z., Liu, G., Wang, J., 2016. Experimental comparisons of dynamic properties of floating wind turbine systems based on two different rotor concepts. Appl. Ocean Res. 58, 266–280. https://doi.org/10.1016/j.apor.2016.04.012.
Edirisinghe, D.S., Yang, H.-S., Gunawardane, S.D.G.S.P., Alkhabbaz, A., Tongphong, W., Yoon, M., et al., 2023. Numerical and experimental investigation on water vortex power plant to recover the energy from industrial wastewater. Renew. Energy 204, 617–634. https://doi.org/10.1016/j.renene.2023.01.007.
Frick, D., Achmus, M., 2020. An experimental study on the parameters affecting the cyclic lateral response of monopiles for offshore wind turbines in sand. Soils Found. 60, 1570–1587. https://doi.org/10.1016/j.sandf.2020.10.004.
Goupee, A.J., Koo, B.J., Kimball, R.W., Lambrakos, K.F., Dagher, H.J., 2014. Experimental comparison of three floating wind turbine concepts. J. Offshore Mech. Arctic Eng. 136 https://doi.org/10.1115/1.4025804.
Häfele, J., Hübler, C., Gebhardt, C.G., Rolfes, R., 2018. A comprehensive fatigue load set reduction study for offshore wind turbines with jacket substructures. Renew. Energy 118, 99–112. https://doi.org/10.1016/j.renene.2017.10.097.
Häfele, J., Gebhardt, C.G., Rolfes, R., 2019. A comparison study on jacket substructures for offshore wind turbines based on optimization. Wind Energy Science 4, 23–40. https://doi.org/10.5194/wes-4-23-2019.
Hamdoon, O., 2020. Improving the performance of A Flat plate solar Collector using Nanofluid as working fluid. Al-Rafidain Engineering Journal (AREJ) 25, 37–45. https://doi.org/10.33899/rengj.2020.127218.1041.
Hansen, M., 2000. Aerodynamics of Wind Turbines. Science Publishers, James and James Ltd.
Hansen, M.O.L., Sørensen, J.N., Voutsinas, S., Sørensen, N., Madsen, HAa, 2006. State of the art in wind turbine aerodynamics and aeroelasticity. Prog. Aero. Sci. 42, 285–330. https://doi.org/10.1016/j.paerosci.2006.10.002.
Henderson, A.R., Morgan, C., Smith, B., Sørensen, H.C., Barthelmie, R.J., Boesmans, B., 2003. Offshore wind energy in Europe— a Review of the state-of-the-art. Wind Energy 6, 35–52. https://doi.org/10.1002/we.82.
Hirt, C.W., Nichols, B.D., 1981. Volume of fluid (VOF) method for the dynamics of free boundaries. J. Comput. Phys. 39, 201–225. https://doi.org/10.1016/0021-9991(81)90145-5.
Intertek, A., Goupee, A., Robertson, A., Kimball, R., Jonkman, J., Swift, A., 2012. FAST Code Verification of Scaling Laws for DeepCwind Floating Wind System Tests. Conference paper, NREL/CP-5000-54221.
Jasim, L., Alkhabbaz, A., Hamzah, H., 2023. Preferred location of the porous sleeve in a concentric annulus depending on the thermal insulation. Proc Inst Mech Eng C J Mech Eng Sci 237. https://doi.org/10.1177/09544062221133940, 2002–13.
Jonkman, J., 2007. Dynamic Modelling and Loads Analysis of an Offshore Floating Wind Turbine. Technical Report NREL/TP-500-41958.
Jonkman, J.M., 2009. Dynamics of offshore floating wind turbines—model development and verification. Wind Energy 12, 459–492. https://doi.org/10.1002/we.347.
Jonkman, J.M., Buhl Jr., M.L., 2005. FAST User's Guide. NREL/TP-500-38230.
Jonkman, J., Butterfield, S., Musial, W., Scott, G., 2009. Definition of a 5-MW Reference Wind Turbine for Offshore System Development. NREL/TP-500-38060.
Jung, S., Kim, S.-R., Patil, A., Hung, L.C., 2015. Effect of monopile foundation modeling on the structural response of a 5-MW offshore wind turbine tower. Ocean Eng. 109, 479–488. https://doi.org/10.1016/j.oceaneng.2015.09.033.
Karimirad, M., Michailides, C., Nematbakhsh, A., 2018. Offshore Mechanics: Structural and Fluid Dynamics for Recent Applications. John Wiley & Sons Ltd.
Kim, J., Shin, H., 2020. Validation of a 750 kW semi-submersible floating offshore wind turbine numerical model with model test data, part II: model-II. Int. J. Nav. Archit. Ocean Eng. 12, 213–225. https://doi.org/10.1016/j.ijnaoe.2019.07.004.
Kim, I.C., Alkhabbaz, A., Jeong, H., Lee, Y.H., 2019. Optimization methodology of small scale horizontal Axis Shrouded tidal current turbine. In: 2019 IEEE Asia-Pacific Conference on Computer Science and Data Engineering (CSDE). IEEE, pp. 1–3. https://doi.org/10.1109/CSDE48274.2019.9162407.
Larsen, J., Dancy, H., 1983. Open boundaries in short wave simulations — a new approach. Coastal Engineering 7, 285–297. https://doi.org/10.1016/0378-3839(83)90022-4.
Lee, C., Newman, J., Kim, M., Yue, D., 1991. The computation of second-order wave loads. Int. Conference on offshore Mechanics and Arctic Engineering 113–123. Norway.
Leimeister, M., Kolios, A., Collu, M., Thomas, P., 2020. Design optimization of the OC3 phase IV floating spar-buoy, based on global limit states. Ocean Eng. 202, 107186 https://doi.org/10.1016/j.oceaneng.2020.107186.
Lerch, M., De-Prada-Gil, M., Molins, C., 2019. The influence of different wind and wave conditions on the energy yield and downtime of a Spar-buoy floating wind turbine. Renew. Energy 136, 1–14. https://doi.org/10.1016/j.renene.2018.12.096.
Li, H., Bachynski, E.E., 2021. Experimental and numerical investigation of nonlinear diffraction wave loads on a semi-submersible wind turbine. Renew. Energy 171, 709–727. https://doi.org/10.1016/j.renene.2021.02.152.
Li, Y., Castro, A.M., Sinokrot, T., Prescott, W., Carrica, P.M., 2015. Coupled multi-body dynamics and CFD for wind turbine simulation including explicit wind turbulence. Renew. Energy 76, 338–361. https://doi.org/10.1016/j.renene.2014.11.014.
Liu, Y., Xiao, Q., Incecik, A., Wan, D., 2016. Investigation of the effects of platform motion on the aerodynamics of a floating offshore wind turbine. J. Hydrodyn. 28, 95–101. https://doi.org/10.1016/S1001-6058(16)60611-X.
Liu, Y., Xiao, Q., Incecik, A., Peyrard, C., Wan, D., 2017. Establishing a fully coupled CFD analysis tool for floating offshore wind turbines. Renew. Energy 112, 280–301. https://doi.org/10.1016/j.renene.2017.04.052.
Ma, K., Luo, Y., Kwan, T., Wu, Y., 2019. Mooring System Engineering for Offshore Structures. Gulf professional publishing is an imprint of Elsevier.
Martin, H., 2009. Development of a Scale Model Wind Turbine for Testing of Offshore Wind Turbine System. M.S. Thesis. University of Maine, Main.
Martinez, A., Iglesias, G., 2022. Mapping of the levelised cost of energy for floating offshore wind in the European Atlantic. Renew. Sustain. Energy Rev. 154, 111889 https://doi.org/10.1016/j.rser.2021.111889.
Masciola, M., Robertson, A., Jonkman, J., Coulling, A., Goupee, A., 2013. Assessment of the Importance of Mooring Dynamics on the Global Response of the DeepCwind Floating Semisubmersible Offshore Wind Turbine. Int. Society of Offshore and Polar Engineers, pp. 359–368.
Masciola, M., Jonkman, J., Robertson, A., 2014. Extending the Capabilities of the Mooring Analysis Program: A Survey of Dynamic Mooring Line Theories for Integration into FAST. NREL\CP-5000-61159.
Musial, W., Butterfield, S., 2004. Future for Offshore Wind Energy in the United States. NREL/CP-500-36313. Florida, USA.
Myhr, A., Maus, K., 2011. Experimental and computational comparisons of the OC3-HYWIND and Tension-Leg-Buoy (TLB) floating wind turbine conceptual designs. Int. Society of Offshore and Polar Engineers 96.
Myhr, A., Nygaard, T., 2014. Experimental results for tension-leg-buoy offshore wind turbine platforms. Int. Society of Offshore and Polar Engineers 4, 217–224.
Myhr, A., Nygaard, T., 2015. Comparison of experimental results and Computations for tension-leg-buoy offshore wind turbines. Int. Society of Offshore and Polar Engineers 2, 12–20.
Nematbakhsh, A., Bachynski, E.E., Gao, Z., Moan, T., 2015. Comparison of wave load effects on a TLP wind turbine by using computational fluid dynamics and potential flow theory approaches. Appl. Ocean Res. 53, 142–154. https://doi.org/10.1016/j.apor.2015.08.004.

Orcina, Ltd, 2012. OrcaFlex Manual, Version 9.6a, p. 474.
Pantusa, D., Tomasicchio, G.R., 2019. Large-scale offshore wind production in the Mediterranean Sea. Cogent Eng 6. https://doi.org/10.1080/23311916.2019.1661112.
Pantusa, D., Francone, A., Tomasicchio, G.R., 2020. Floating offshore renewable energy farms. A Life-cycle cost analysis at Brindisi. Italy. Energies (Basel) 13, 6150. https://doi.org/10.3390/en13226150.
Patanker, S., 1980. Numerical Heat Transfer and Fluid Flow. McGRAW-Hill Book Company.
Robertson, A., Jonkman, J., Masciola, M., Song, H., Goupee, A., Coulling, A., Luan, C., 2014. Definition of the Semisubmersible Floating System for Phase II of OC4. NREL/TP-5000-60601.
Roddier, D., Cermelli, C., Aubault, A., Weinstein, A., 2010. WindFloat: a floating foundation for offshore wind turbines. J. Renew. Sustain. Energy 2. https://doi.org/10.1063/1.3435339.
Rodriguez, S.N., Jaworski, J.W., 2020. Strongly-coupled aeroelastic free-vortex wake framework for floating offshore wind turbine rotors. Part 2: application. Renew. Energy 149, 1018–1031. https://doi.org/10.1016/j.renene.2019.10.094.
Sebastian, T., Lackner, M.A., 2013. Characterization of the unsteady aerodynamics of offshore floating wind turbines. Wind Energy 16, 339–352. https://doi.org/10.1002/we.545.
Segura, E., Morales, R., Somolinos, J.A., 2018. A strategic analysis of tidal current energy conversion systems in the European Union. Appl. Energy 212, 527–551. https://doi.org/10.1016/j.apenergy.2017.12.045.
Shan, T., Yang, J., Li, X., Xiao, L., 2011. Experimental investigation on wave run-up characteristics along columns and air gap response of semi-submersible platform. J. Hydrodyn. 23, 625–636. https://doi.org/10.1016/S1001-6058(10)60158-8.
Shi, W., Han, J., Kim, C., Lee, D., Shin, H., Park, H., 2015. Feasibility study of offshore wind turbine substructures for southwest offshore wind farm project in Korea. Renew. Energy 74, 406–413. https://doi.org/10.1016/j.renene.2014.08.039.
Soukissian, T., Karathanasi, F., Axaopoulos, P., 2017. Satellite-based offshore wind resource assessment in the Mediterranean sea. IEEE J. Ocean. Eng. 42, 73–86. https://doi.org/10.1109/JOE.2016.2565018.
Stewart, G., Muskulus, M., 2016a. A review and comparison of floating offshore wind turbine model experiments. Energy Proc. 94, 227–231. https://doi.org/10.1016/j.egypro.2016.09.228.
Stewart, G., Muskulus, M., 2016b. A review and comparison of floating offshore wind turbine model experiments. Energy Proc. 94, 227–231. https://doi.org/10.1016/j.egypro.2016.09.228.
Tian, C., Liu, M., Xiao, L., Goncalves, R.T., Xie, W., Wang, S., 2021. Effects of the position of pipe-type appendages on the flow induced motions, energy transformation, and drag force of a TLP. Appl. Ocean Res. 106, 102464 https://doi.org/10.1016/j.apor.2020.102464.
Toan Tran, T., Kim, D.-H., Hieu Nguyen, B., 2015. Aerodynamic interference effect of huge wind turbine blades with periodic surge motions using overset grid-based computational fluid dynamics approach. J. Sol. Energy Eng. 137 https://doi.org/10.1115/1.4031184.
Tomasicchio, G., D'Alessandro, F., Avossa, A., Riefolo, L., Musci, E., Ricciardelli, F., Vicinanza, D., 2018. Experimental modelling of the dynamic behavior of a spar buoy wind turbine. Renew. Energy 127, 412–432. https://doi.org/10.1016/j.renene.2018.04.061.
Tran, T.T., Kim, D.-H., 2015a. The coupled dynamic response computation for a semi-submersible platform of floating offshore wind turbine. J. Wind Eng. Ind. Aerod. 147, 104–119. https://doi.org/10.1016/j.jweia.2015.09.016.
Tran, T.T., Kim, D.H., 2015b. The aerodynamic interference effects of a floating offshore wind turbine experiencing platform pitching and yawing motions. J. Mech. Sci. Technol. 29, 549–561. https://doi.org/10.1007/s12206-015-0115-0.
Tran, T.T., Kim, D.-H., 2016a. Fully coupled aero-hydrodynamic analysis of a semi-submersible FOWT using a dynamic fluid body interaction approach. Renew. Energy 92, 244–261. https://doi.org/10.1016/j.renene.2016.02.021.
Tran, T.T., Kim, D.-H., 2016b. A CFD study into the influence of unsteady aerodynamic interference on wind turbine surge motion. Renew. Energy 90, 204–228. https://doi.org/10.1016/j.renene.2015.12.013.
User Manual, STAR-CCM+, version 15.02.
Utsunomiya, T., Sato, T., Matsukuma, H., Yago, K., 2009. Experimental Validation for Motion of a SPAR-type Floating Offshore Wind Turbine Using 1/22.5 Scale Model, vol. 4. Ocean Engineering; Ocean Renewable Energy; Ocean Space Utilization, Parts A and B, ASMEDC, pp. 951–959. https://doi.org/10.1115/OMAE2009-79695.
Versteeg, H., Malalasekera, W., 2007. An Introduction to Computational Fluid Dynamics: the Finite Volume Method, second ed. Pearson Education Limited.
Vicente, P.C., de, O., Falcão, A.F., Gato, L.M.C., Justino, P.A.P., 2009. Dynamics of arrays of floating point-absorber wave energy converters with inter-body and bottom slack-mooring connections. Appl. Ocean Res. 31, 267–281. https://doi.org/10.1016/j.apor.2009.09.002.
Viviano, A., Naty, S., Foti, E., Bruce, T., Allsop, W., Vicinanza, D., 2016. Large-scale experiments on the behaviour of a generalised Oscillating Water Column under random waves. Renew. Energy 99, 875–887. https://doi.org/10.1016/j.renene.2016.07.067.
Ward, J.C., Goupee, A.J., Viselli, A.M., Dagher, H.J., 2021. Experimental investigation into the dynamic behavior of a floating offshore wind turbine stabilized via a suspended counterweight. Ocean Eng. 228, 108906 https://doi.org/10.1016/j.oceaneng.2021.108906.
Wiegard, B., König, M., Lund, J., Radtke, L., Netzband, S., Abdel-Maksoud, M., et al., 2021. Fluid-structure interaction and stress analysis of a floating wind turbine. Mar. Struct. 78, 102970 https://doi.org/10.1016/j.marstruc.2021.102970.
Wu, H., Zhao, Y., He, Y., Shao, Y., Mao, W., Han, Z., et al., 2021. Transient response of a TLP-type floating offshore wind turbine under tendon failure conditions. Ocean Eng. 220, 108486 https://doi.org/10.1016/j.oceaneng.2020.108486.
Xiong, X.-L., Lyu, P., Chen, W.-L., Li, H., 2020. Self-similarity in the wake of a semi-submersible offshore wind turbine considering the interaction with the wake of supporting platform. Renew. Energy 156, 328–341. https://doi.org/10.1016/j.renene.2020.04.071.
Yang, H.-S., Alkhabbaz, A., Edirisinghe, D.S., Tongphong, W., Lee, Y.-H., 2022. FOWT stability study according to number of columns considering amount of materials used. Energies 15, 1653. https://doi.org/10.3390/en15051653.
Yang, H.-S., Tongphong, W., Ali, A., Lee, Y.-H., 2023. Comparison of different fidelity hydrodynamic-aerodynamic coupled simulation code on the 10 MW semi-submersible type floating offshore wind turbine. Ocean Eng. 281, 114736 https://doi.org/10.1016/j.oceaneng.2023.114736.
Zhang, M., Li, X., Tong, J., Xu, J., 2020. Load control of floating wind turbine on a Tension-Leg-Platform subject to extreme wind condition. Renew. Energy 151, 993–1007. https://doi.org/10.1016/j.renene.2019.11.093.
Zhao, W., Wan, D., 2015. Numerical study of interactions between phase II of OC4 wind turbine and its semi-submersible floating support system. Int. Society of Offshore and Polar Engineers 2, 45–53.
Zhou, L., Li, Y., Liu, F., Jiang, Z., Yu, Q., Liu, L., 2019. Investigation of dynamic characteristics of a monopile wind turbine based on sea test. Ocean Eng. 189, 106308 https://doi.org/10.1016/j.oceaneng.2019.106308.